Check for updates

Graphene-Ta$_2$O$_5$ heterostructure enabled high performance, deep-ultraviolet to mid-infrared photodetection†

Vinh X. Ho,[a] Yifei Wang,[a] Michael P. Cooney[b] and N. Q. Vinh ⓘ *[a]

Ultrafast, high sensitive, low cost photodetectors operating at room temperature sensitive from the deep-ultraviolet to mid-infrared region remain a significant challenge in optoelectronics. Achievements in traditional semiconductors using cryogenic operation and complicated growth processes prevent the cost-effective and practical application of broadband detectors. Alternative methods towards high-performance photodetectors, hybrid graphene-semiconductor colloidal quantum dots have been intensively explored. However, the operation of these photodetectors has been limited by the spectral bandwidth and response time. Here, we have demonstrated hybrid photodetectors operating from the deep-ultraviolet to the mid-infrared region with high sensitivity and ultrafast response by coupling graphene with a p-type semiconductor photosensitizer, nitrogen-doped Ta$_2$O$_5$ thin film. Photons with energy higher than the energy of the defect centers release holes from neutral acceptors. The holes are transferred into graphene, leaving behind ionized acceptors. Due to the advantage of two-dimensional heterostructure including homogeneous thickness, extending in a two-dimensional plane, large contact area between the N-Ta$_2$O$_5$ thin film and graphene, and the high mobility of carriers in graphene, holes are transferred rapidly to graphene and recirculated during the long lifetime of ionized acceptors. The photodetectors achieve a high photo-responsivity (up to 3.0 × 10^6 A W^{-1}), ultrafast rise time (faster than 20 ns), and a specific detectivity (up to ~2.2 × 10^{12} Jones). The work provides a method for achieving high-performance optoelectronics operating in the deep-ultraviolet to mid-infrared region.

[a]*Department of Physics and Center for Soft Matter and Biological Physics, Virginia Tech, Blacksburg, VA 24061, USA. E-mail: vinh@vt.edu; Tel: +1-540-231-3158*
[b]*NASA Langley Research Center, Hampton, Virginia 23681, USA*
†Electronic supplementary information (ESI) available. See DOI: 10.1039/d1nr01572a

Introduction

The capability to convert light into electrical signals over a broad spectral range with high sensitivity and low cost is central to many technological applications including video imaging, night-vision, security, optical communication, sensing, and spectroscopy.[1,2] Graphene has been exhibited as a potential optoelectronic material for broadband photodetectors from the deep-ultraviolet (UV) to the terahertz (THz) region.[1–3] Unfortunately, due to the fast carrier recombination rate on the picosecond time-scale,[4] as well as the intrinsic low absorption of graphene,[5] photodetectors based on graphene suffer from poor detectivity as well as low photo-responsivity, preventing use in broadband applications. To enhance the light absorption, graphene is usually hybridized with other nanostructures for graphene-based photodetectors.[6,7] Among

these nanostructures, the ultrahigh photoconductive gain was obtained in hybrid colloidal quantum dots (CQDs) on graphene, where graphene acts as an ultrafast carrier transport channel and CQDs are used as an ultrahigh photon absorbing material. In these hybrid nanoscale structures, charge carriers are generated from light-absorbing CQDs. Electrons or holes are trapped in the CQDs, while the oppositely charged carriers transfer to graphene and rapidly recirculate in the graphene channel controlled by a drain–source bias voltage, leading to a photogating effect.[8,9] Depending on CQDs, graphene hybrid photodetectors have shown a high sensitivity photodetection from the UV to near-infrared (NIR) region. However, graphene-CQD photodetectors face a limited spectral bandwidth due to the large energy of exciton peaks,[6,9] and a long response time in the sub-millisecond to second time-scale.[9–11]

The ultrahigh photoconductive gain of graphene-CQD photodetectors originates from the long lifetime of trapped-charge carriers remaining in CQDs and the high carrier mobility (μ = 60 000 cm^2 s^{-1} V^{-1})[12] of graphene sheet at room temperature on a substrate. The gain can be determined based on a simple approximation of the trapped-charge carrier lifetime, $\tau_{\text{trapped carrier}}$, of electron or hole, and the transit time, τ_{transit},

of the opposite type carrier given by $G = \tau_{\text{trapped carrier}}/\tau_{\text{transit}}$.[9] For graphene-CQD photodetectors, the photo-responsivity is up to $\sim 1 \times 10^9$ A W^{-1} in the visible region[6,9,11] while the response time is very slow (in the order of ~ 10 ms or longer) due to the long lifetime of carriers trapped in the CQDs. The ultrahigh gain has been observed in many types of hybrid structures including graphene–PbS,[6,9,10] graphene–TiO$_2$,[13] graphene–ZnO,[14] graphene–Si,[11,15] and graphene–chlorophyll (biological material).[16] The long lifetime of trapped-charge carriers provides an ultrahigh gain, but, leading to a slow response time of the photodetectors. The transfer time of carriers from CQDs to graphene strongly depends on the surface properties of CQDs, and the contact area between CQDs and graphene. Thus, to increase the operation speed in the graphene-CQD photodetectors, a reset voltage pulse applied to the back-gate has been used to purge charge carriers from CQDs.[7,9]

To obtain an ultrahigh photoconductive gain as well as a fast operation time, including response and recovery time of graphene-based photodetectors, we have employed a two-dimensional (2D) light-absorbing layer, a p-type semiconductor photosensitizer, nitrogen-doped tantalum oxide (N-Ta$_2$O$_5$). The N-Ta$_2$O$_5$ layer has a thickness of 10 nm grown by electron beam evaporation containing electron acceptor impurities atop graphene. Recently, this material has been used in a wide range of applications in solar energy conversion and microelectronics including photocatalytic materials,[17] charge-trapping for nonvolatile resistive random access memories,[18] atomic switches,[19] capacitors, insulators,[20,21] thin-film electroluminescent devices,[22] and high-speed elements due to their high dielectric constant ($\kappa = 25$–40), and good thermal and chemical stability. The N-Ta$_2$O$_5$ light-absorbing thin film contains defects (acceptor impurities), acting like negative charge centers. The long lifetime of charge centers provides an ultrahigh gain for the photodetectors, similar to the graphene-CQD photodetectors. Due to the nature of 2D heterostructure (instead of quantum dots) including homogeneous thickness, extending in a 2D plane, and large contact area between the N-Ta$_2$O$_5$ thin film and graphene, carriers are transferred rapidly and efficiently to graphene. Also, ionized acceptor impurities of the 2D light-absorbing layer will be neutralized quickly when the light source is turned off. The devices exhibit a significantly high photo-responsivity of $\sim 3.0 \times 10^6$ A W^{-1} in the UV-to-NIR region, and ~ 7.2 A W^{-1} in the mid-infrared (MIR) region. A fast rise time of 20 ns or a high electrical bandwidth of ~ 50 MHz has been observed.

Results and discussion

The active area of the graphene-Ta$_2$O$_5$ photodetectors consists of a graphene sheet and a 10 nm N-Ta$_2$O$_5$ layer. Graphene acts as a carrier transport channel with the N-Ta$_2$O$_5$ thin film used as an enhanced photon absorbing material containing ionized acceptors. The active area is placed on top of a Si/SiO$_2$ wafer as illustrated in Fig. 1a (see Materials and methods as well as ESI† for details of the device fabrication).[23–25] To compare

with earlier findings for graphene-based photodetectors, where the photocurrent occurs with the presence of charges in CQDs changing the graphene sheet resistance,[9,11,13] in the vicinity of a p–n junction,[26,27] in heterojunctions,[28] at the interface of graphene and metal contacts,[5] a thin tunnel barrier,[7] our structure based on the field effect transistor (FET) shows a fast photo-response with the N-Ta$_2$O$_5$ thin film, a decrease in the noise level, and is well protected from the top Al$_2$O$_3$ layer. The Ta$_2$O$_5$ layer was doped with nitrogen to form acceptor centers[29–38] using the electron beam (e-beam) evaporation deposition. The device was transferred to an atomic layer deposition chamber to grow a 30 nm Al$_2$O$_3$ layer on top. The N-Ta$_2$O$_5$ layer contains acceptor centers with energy levels in the band gap of the material. Acceptor centers are ionized by absorbing photons with energy higher than the energy of the defects, resulting in hole generation. The holes are transferred rapidly into the graphene channel, leaving behind ionized acceptors (negative charges). Due to the high carrier mobility in graphene, holes are recirculated during the long lifetime of ionized acceptors. The graphene-Ta$_2$O$_5$ heterostructure offers a large spectral sensitivity from the deep-UV to MIR region with very fast operation time.

Nitrogen incorporation into oxides is widely reported in the literature, and N-doped Ta$_2$O$_5$ exhibits a dual functional modulation including band gap narrowing and p-type conduction.[29–40] A number of studies including absorption experiments and X-ray photoelectron spectroscopy,[30–32] ultraviolet photoelectron spectroscopy and electrochemical techniques,[33] time-resolved spectroscopic studies,[34] and density-functional theory calculations[35,36,40] have shown that Ta$_2$O$_5$ phase changes to p-type in the nitrogen-doped Ta$_2$O$_5$ material. Nitrogen doping in Ta$_2$O$_5$ increases the number of defect states and produces multiple levels (or a band) above the valence band (VB) of ~ 1.25 eV from the N 2p orbital, and the oxygen sites are substituted by nitrogen atoms.[34,39,40] The N 2p states form a band above the VB, resulting in band gap narrowing and p-type conduction. To verify the optical properties of the N-Ta$_2$O$_5$ material, absorption spectra have been collected in the UV-visible as well as in the NIR to MIR regions (Fig. S5 in the ESI†) for 100 nm N-Ta$_2$O$_5$ layers. Note that to obtain better signals of absorption spectra in a large range of wavelengths (200 nm to 22 μm), 100 nm N-Ta$_2$O$_5$ layers were grown on different substrates. For the visible region, a 100 nm N-Ta$_2$O$_5$ layer was grown on a sapphire substrate, and for the infrared region this material was grown on a silicon substrate. The observation (Fig. S5†) is similar with previous reports in the literature.[30–32] The band gap of the N-Ta$_2$O$_5$ material becomes narrower (Fig. S5b†), and the infrared absorption spectrum (Fig. S5a†) shows a strong absorption in the infrared region with the maximum around 1 eV, and a long tail extending to the MIR region. The broad band of defect levels near the valence band of N-Ta$_2$O$_5$ is supported by calculations of the density-functional theory (DFT).[36,40] Several peaks at the long wavelength come from vibrational modes in the material (they are not electronic transitions), indicating the formation of the Ta$_2$O$_5$ material (Fig. S5, ESI†).
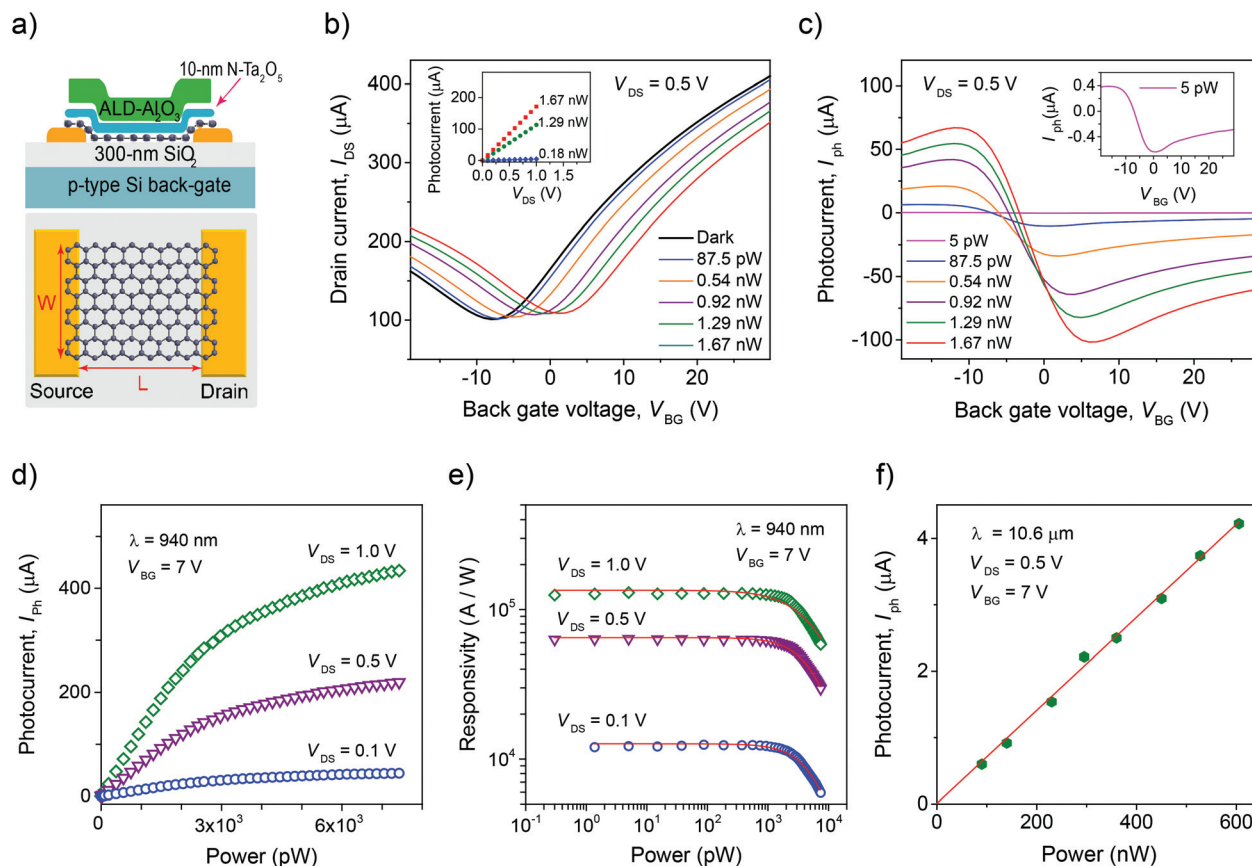
Fig. 1 Graphene-Ta_2O_5 hybrid thin film photodetector. (a) Schematic of the phototransistor showing source, drain, back-gate contacts together with graphene, 10 nm N-Ta_2O_5, and 30 nm Al_2O_3 layers. (b) I–V_{BG} characteristics of the graphene-Ta_2O_5 photodetector under different illumination powers, V_{DS} = 0.5 V. The wavelength is 940 nm with a spot size of 5 mm, covering the entire photodetector. Inset: The photocurrent increases linearly with the drain–source bias voltage under V_{BG} = 7.0 V. (c) Photocurrent curves under different illumination powers as a function of back-gate voltage. The magnitude of photocurrent increases with illumination power. (d) Power dependence of photocurrent at V_{BG} = 7.0 V for three values of the drain–source voltage, V_{DS}, of 0.1, 0.5 V, and 1 V. The photocurrent increases linearly with light intensity, and grows slowly at high illumination power. (e) The photo-responsivity shows a constant value at low illumination power and reduces at high excitation power. The solid curves are the best fit to the data using the function in eqn (1). (f) Power dependence of photocurrent using a CO_2 laser (λ = 10.6 μm) for excitation at V_{BG} = 7.0 V. A linear increase of photocurrent with illumination power has been observed.

The effect of light illumination on the graphene-Ta_2O_5 heterostructure photodetector with the gap between drain and source contacts (or the length), L, of 30 μm, and the width of the active area, W, of 30 μm (W/L = 1) is shown in the Fig. 1. Specifically, we have observed the drain–source current, I_{DS}, with and without illumination of a laser diode operating at 940 nm as a function of the back-gate voltage, V_{BG}. The power of the pump laser was varied from 300 fW to 7.5 nW. Fig. 1b shows transfer characteristic (I–V) curves of the device for the drain–source bias voltage, V_{DS}, of 0.5 V. A shift of the charge neutrality point (CNP) voltage (V_{Dirac}) of the transfer characteristic curves toward positive of the back-gate voltage, V_{BG}, has been observed with increasing illumination power. The photocurrent increases for $V_{BG} < V_{Dirac}$ where the carrier transport is hole-dominated. In this case, photo-generated holes were transferred from the N-Ta_2O_5 thin film to graphene, leaving behind ionized acceptors. Thus, a high photocurrent has been observed. For $V_{BG} > V_{Dirac}$, where the carrier transport is elec-

tron-dominated, the illumination leads to a decrease in dark current (or a negative photocurrent) due to the recombination taking place between holes transferred from the N-Ta_2O_5 layer to graphene and electrons induced by the back-gate. As long as acceptors in the 10 nm N-Ta_2O_5 layer remain ionized (negative charge), holes in the graphene layer are recirculated, resulting in a photoconductive gain in the graphene-Ta_2O_5 heterostructure device.

By subtracting the dark-current from the illumination-current, we can determine the net photocurrent (I_{ph} = $I_{illumination}$ – I_{dark}) of the device. The photocurrent curves under different illumination powers are plotted in Fig. 1c. A net photocurrent of ~100 μA has been observed at V_{BG} = 7 V and V_{DS} = 0.5 V. The photocurrent curves demonstrate that the magnitude of the photocurrent increases with illumination power.

To gain insight into the characteristics of the graphene-Ta_2O_5 heterostructure, we carried out the power dependence of

the photocurrent (Fig. 1d) as well as determined the photo-responsivity (Fig. 1e), $R_{ph} = I_{ph}/P$, of the photodetector under the 940 nm illumination, at $V_{BG} = 7.0$ V for three values of the drain–source voltage, V_{DS}, of 0.1, 0.5, and 1 V. Under low illumination power of 300 fW, the device shows a photo-responsivity of 1.25×10^5 A W^{-1}, suggesting that graphene and Ta$_2$O$_5$ layers efficiently convert photon energy into a large electrical current. The power dependence of the positive and negative photocurrent shows a similar behavior. The photocurrent increases linearly with illumination power from 300 fW to ~2 nW (almost four orders of magnitude) and grows slowly at high illumination power. In an equivalent way, the photo-responsivity shows a constant value at low illumination power and reduces after that (Fig. 1e). The photo-responsivity reduces from 1.25×10^5 to 5.85×10^4 A W^{-1} when the excitation power is higher than 2 nW. At low illumination power, ionized acceptors in the N-Ta$_2$O$_5$ layer are well separated from photon-generated holes, thus a high gain from the photogating effect has been obtained. As we increase the illumination power, a higher concentration of carriers (electrons and holes) is introduced. Ionized acceptor centers (negative charges) can be recombined with holes in the picosecond time-scale.[4] These holes will not take part in the charge transfer process, and thus, the photo-responsivity reduces as well as the average lifetime of ionized acceptors is shortened at high illumination power.

The photo-responsivity of photodetectors strongly depends on the carrier dynamics. The carrier lifetime can be expressed as a function of illumination power, $T_{carrier} = T_0/(1 + (P/P_0)^m)$, T_0 is the lifetime of trapped-charge carriers at low illumination power ($P \to 0$), P_0 is the illumination power in which acceptor centers are fully ionized, and m is a phenomenological fitting parameter ($m \approx 1$). Due to the high mobility of carriers in graphene, holes will recirculate between drain and source electrodes many times during the long lifetime of the ionized acceptors, resulting in a high photo-responsivity or a high gain. The photocurrent can be defined as $I_{ph} = q\alpha\eta N_{ph}T_{carrier}/(L/V)$, where q is the elementary charge, α is the carrier transfer efficiency from the N-Ta$_2$O$_5$ thin film to graphene, η is the internal quantum efficiency of the carrier photo-generation in the N-Ta$_2$O$_5$ thin film layer, N_{ph} is the number of photons absorbed per unit time, and $V = \mu V_{DS}L^{-1}$ is the carrier drift velocity. For a device with $L = 30$ μm, $V_{DS} = 1.0$ V, and the carrier mobility, μ, of ~4850 cm^2 s^{-1} V^{-1},[41] the average of carrier transit time in the graphene channel, $T_t = (L/V)/2 = L^2\mu^{-1}V_{DS}^{-1}/2$, is estimated to be ~0.93 ns. The gain of this hybrid structure can be determined, thusly:[9,42]

$$G = \frac{N_{hole}}{N_{ph}} = \frac{I_{ph}/q}{P/h\nu} = R_{ph}\frac{h\nu}{q} = \alpha\eta\left(\frac{T_0}{T_t}\right)\frac{1}{1 + (P/P_0)^m}, \quad (1)$$

where $h\nu$ is the photon energy. The first term of eqn (1) is the expression for the gain, which is defined as the ratio of the trapped-charge carrier lifetime at low illumination power to the carrier transit time, and the second term regards for the full ionization of acceptor centers at high illumination power.

The long lifetime of ionized acceptors combined with the fast carrier transit time results in a high photo-responsivity $R_{ph} = 1.25 \times 10^5$ A W^{-1} (or a gain of 1.65×10^5). The decrease of the gain at high illumination power is an indication of full ionization. The solid lines are fitting curves to experimental data with $P_0 = $ ~2.1 nW and $m \sim 1.15$.

To examine the MIR response, experiments were conducted with a CO$_2$ laser ($\lambda = 10.6$ μm, $V_{DS} = 0.5$ V, $V_{BG} = 7$ V). The photocurrent as a function of illumination power is shown in Fig. 1f. A linear behavior of the photocurrent with the illumination power has been observed. From the results, the photo-responsivity in the MIR region of 7.2 A W^{-1} has been obtained. In addition, the photocurrent shows a linear dependence on the drain–source bias voltage, V_{DS} (Fig. 1b, inset), suggesting that higher photo-responsivity can be readily obtained by applying a higher bias voltage. As can be seen from Fig. 1(d and e), with $V_{BG} = 7.0$ V, the photo-responsivity of the device at $V_{DS} = 1.0$ V is higher than those from a lower voltage between drain and source.

The photo-responsivity depends strongly on physical parameters of the devices. Specifically, the photo-responsivity depends on the geometrical parameters including the length, L, and the width, W, of the active area. A simple electrical circuit has been developed for the graphene photodetectors:[43]

$$I_{ph} = I_{illumination} - I_{dark} = \frac{V_{DS}}{R_0 + R_{illu}} - \frac{V_{DS}}{R_0 + R_D}, \quad (2)$$

where R_0, R_{illu} and R_D are the contact resistance, the resistance of the active area with and without light illumination, respectively. The sheet resistance of the active area under the dark condition can be calculated as:

$$R_D = \frac{L/W}{nq\mu}, \quad (3)$$

where n is the carrier concentration in the graphene-Ta$_2$O$_5$ layer. Inset in Fig. 2a shows the dark current at the CNP (the minimum current of transfer characteristic curves) as a function of length, L, for $W/L = 2$. With $V_{DS} = 0.5$ V, the total resistance under the dark condition, R_D, is ~2.7 kΩ. The dark resistance value is close with other reports.[6,9,14] When the device is illuminated, a number of carriers are generated from the N-Ta$_2$O$_5$ light-absorbing layer and transferred to electrodes. Δn is the carrier concentration variation in the active area of the device. The photocurrent for low illumination power is solved as:[43]

$$I_{ph} = \frac{V_{DS}}{R_0 + \dfrac{W/L}{(n + \Delta n)e\mu}} - \frac{V_{DS}}{R_0 + \dfrac{W/L}{ne\mu}}$$
$$\approx \frac{V_{DS}\Delta ne\mu}{(R_0 ne\mu(W/L) + 1)^2}(W/L) \quad (4)$$

Fixing the ratio of the width and the length (W/L), the photocurrent, I_{ph}, is proportional to the carrier concentration variation, Δn. Thus, to increase the photo-responsivity of the detector, reducing the active area will enhance the carrier concentration variation, Δn. Fig. 2a shows that for a fixed ratio of
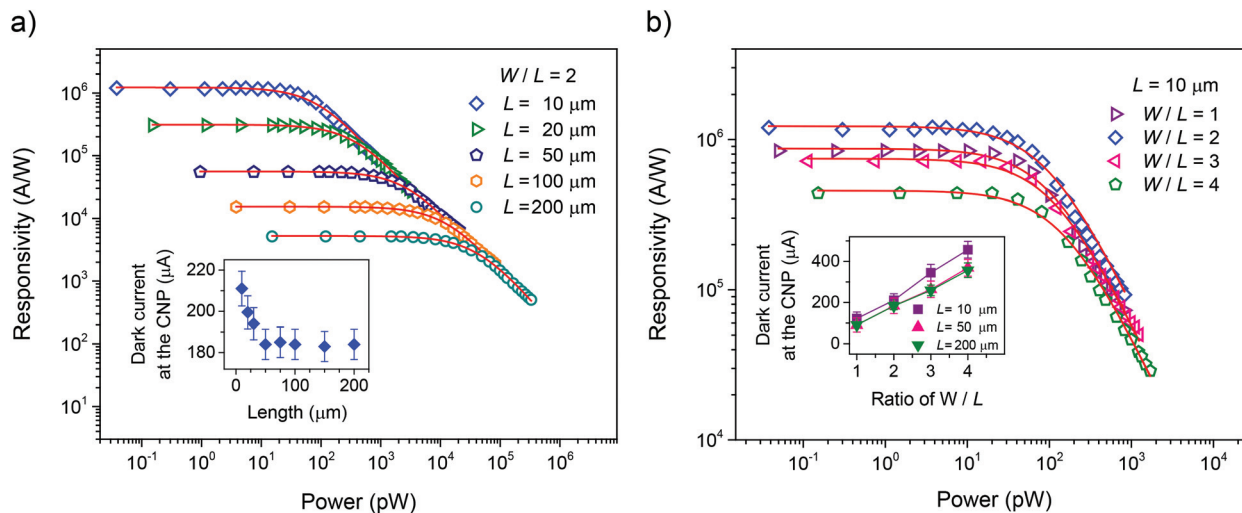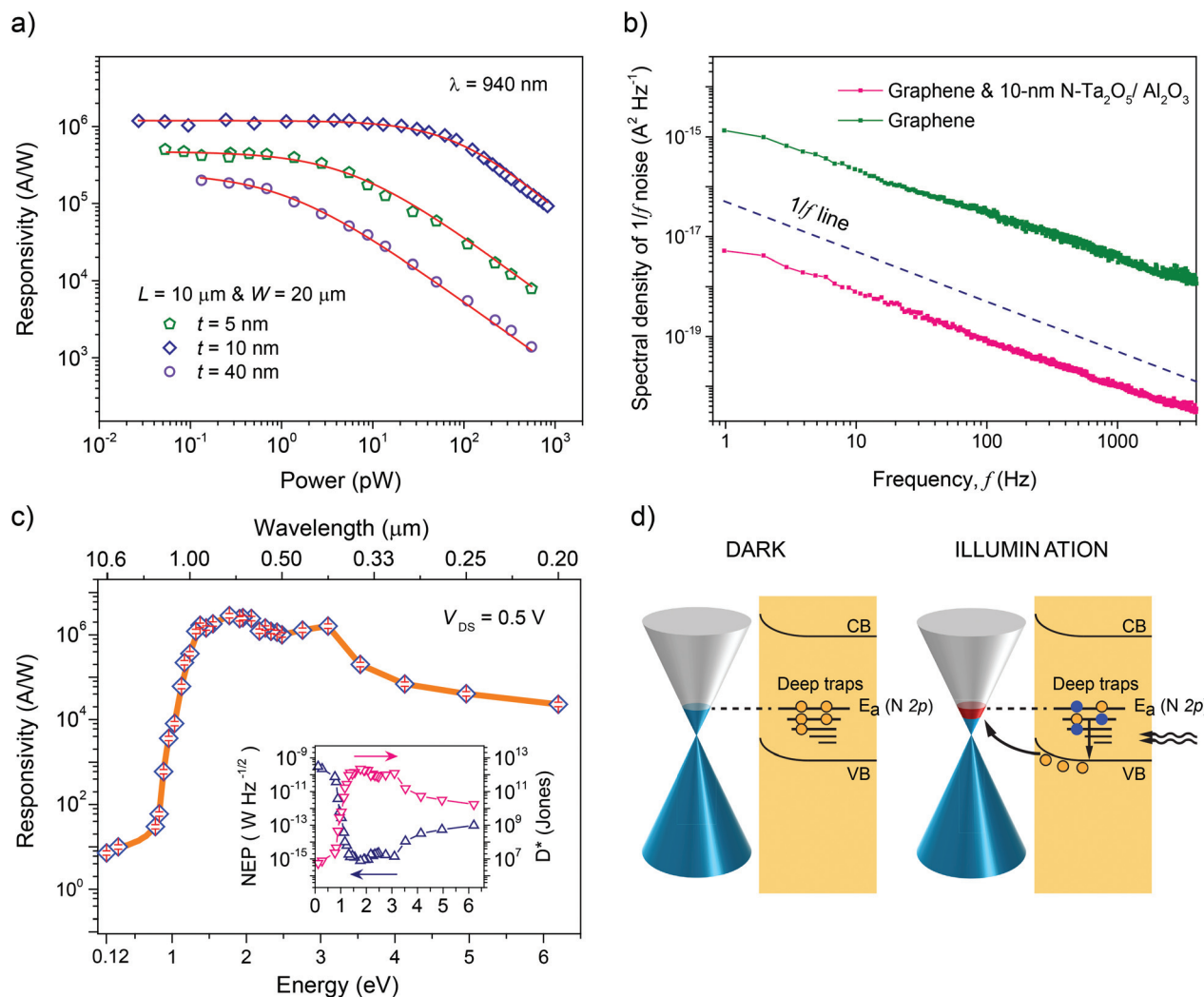
Fig. 2 The measured photo-responsivity for photodetectors with different graphene sheet dimensions under V_{DS} = 0.5 V and V_{BG} = 7.0 V. (a) The measured photo-responsivity of photodetectors for the ratio W/L = 2 with different lengths, L, as a function of illumination power. The solid curves are the best fit to the data using the function in eqn (1). Inset: The dark current at the charge neutrality point as a function of length, L. The dark current increases significantly when the length becomes shorter. (b) The measured photo-responsivity for L = 10 μm with different ratios W/L as a function of illumination power. Inset: The dark current at the charge neutrality point as a function of the ratio of W/L.

W/L = 2, the photo-responsivity increases several orders of magnitude from $W \times L$ = 400 × 200 μm2 to the $W \times L$ = 20 × 10 μm2, under V_{BG} = 7 V and V_{DS} = 0.5 V. When the active area was reduced with a fixed W/L ratio, the length, L, also was reduced. With a shorter length, the dark current increases significantly (Fig. 2a, inset), reducing the performance of the device.

A smaller active area provides a high photo-responsivity, however, the dark-current, I_D, as well as the photocurrent, I_{ph}, vary with the width, W, of the active area.[43] For a fixed length, L, the dark current (inset in Fig. 2b) as well as the photocurrent increase when the width, W, increases. To optimize the performance, characterization of the photo-responsivity was performed with different W/L ratio for L = 10 μm, i.e., $W \times L$ = 10 × 10 μm2, $W \times L$ = 20 × 10 μm2, $W \times L$ = 30 × 10 μm2, $W \times L$ = 40 × 10 μm2 (Fig. 2b). The highest photo-responsivity was obtained for the $W \times L$ = 20 × 10 μm2 device. With increasing the width, a higher photo-responsivity is obtained. However, increasing the width beyond 20 μm decreases the photo-responsivity. The decreasing photo-responsivity with a width larger than 20 μm is a result of the recombination of carriers at defects on the monolayer graphene. The monolayer graphene was grown on a copper foil by CVD and consists of single-crystalline grains with sizes from 10 to 20 μm.[44] Carriers produced by photon absorption strongly recombine at defects or grain boundaries. Thus, when the width increases, the photocurrent and photo-responsivity were slowly increased. For the best performance, optimal parameters are W = 20 μm and L = 10 μm. With this structure, the photodetector can detect the light intensity as low as 27 fW (0.135 mW m^{-2}) in the near infrared region. Note that the results show a similar behavior for both laser (coherent) and lamp (incoherent) light sources.

The thickness of the N-Ta$_2$O$_5$ layer plays an important factor for the performance of the graphene-Ta$_2$O$_5$ devices. The photo-responsivity increases when the thickness of the N-Ta$_2$O$_5$ layer, t, increases from 5 nm to 10 nm (Fig. 3a), and then the photo-responsivity is lower when the thickness of the N-Ta$_2$O$_5$ layer is thicker (t = 40 nm). The effect of the thickness on the photo-responsivity can be attributed to the trade-off between the light absorption and the charge transfer efficiency. When we increase the thickness of the N-Ta$_2$O$_5$ layer, a high number of optical centers have been obtained, resulting in a higher photo-responsivity. However, as the thickness of the N-Ta$_2$O$_5$ layer is larger than the charge carrier diffusion length, the charge transfer to graphene is inefficient. Thus, the photo-responsivity for a device with the thickness of the N-Ta$_2$O$_5$ layer of 40 nm reduces. Furthermore, to have a thicker N-Ta$_2$O$_5$ layer, the graphene channel might degrade during a longer time of the growing process, and thus reducing the performance of the photodetectors.

To characterize the broadband photo-response of the devices, photo-responsivity as a function of illuminated photon energy was measured. The photo-responsivity shows a broadband spectrum from the MIR to deep-UV region (Fig. 3c). Specifically, the photo-responsivity at the MIR region (10.6 μm or 0.12 eV) is 7.2 A W^{-1}, and is significantly sensitive in the range from the NIR (1.53 μm or 0.81 eV) to the deep-UV (200 nm or 6.2 eV) region on the order of 10^6 A W^{-1}. The light sources used here include a monochromatic light extracted from a broadband deuterium/tungsten lamp (0.19–2.6 μm), laser diodes operating at 532 and 940 nm, a fiber laser lasing at 1.53 μm, a quantum cascade laser lasing at 4.55 μm, and a CO$_2$ laser operating at 10.6 μm. The light source is expanded to a large beam and a pinhole has been used to obtain the photon flux. The spectral photo-responsivity of the device con-

Fig. 3 Spectral sensitivity and detectivity of graphene-Ta$_2$O$_5$ heterostructure devices ($W \times L = 20 \times 10$ μm^2). (a) The measured photo-responsivity of three devices with different thicknesses of the N-Ta$_2$O$_5$ layer under 940 nm excitation wavelength. (b) Power spectral density of 1/f noise in the dark for two devices of graphene-Ta$_2$O$_5$ heterostructure, and graphene only. The dashed line has the slope −1 and shows "pure" 1/f noise. (c) Photo-responsivity of the device as a function of excitation photo-wavelength from 200 nm to 10.6 μm (or from 0.12 to 6.2 eV) under $V_{DS} = 0.5$ V and V_{BG} = 7 V. The blue diamonds are experimental data, and the orange line is a guide to the eye. Inset: Spectral dependence of the NEP and specific detectivity (D^*) of the photodetector device at room temperature. (d) Schematic diagram of energy band structures of graphene and N-Ta$_2$O$_5$ together with the tendency of charge transfer between layers. The blue dots present for the ionized acceptor centers, while hollow dots stand for holes.

taining a 10 nm N-Ta$_2$O$_5$ layer on graphene shows an onset at ~1 eV. As mentioned above, nitrogen doping in Ta$_2$O$_5$ contributes to the optical absorption of the material by two ways including increasing the number of defect states and producing energy levels above the valence band originated from the N 2p orbital. Photons with energy higher than the acceptor energy ionize the accepter centers, resulting in hole generation. Holes transfer rapidly from the N-Ta$_2$O$_5$ layer into graphene channel, leaving behind negative charges (ionized acceptor centers). Furthermore, the N-Ta$_2$O$_5$ thin layer has an amorphous phase, the N 2p states create a broad band with the maximum of photon-ionization cross section at ~1 eV above the VB. The spectral photo-responsivity from the graphene-Ta$_2$O$_5$ heterostructure showed a maximum at ~1 eV and

a long tail extending to the MIR region (Fig. 3c). Fig. 3d demonstrates a schematic diagram of energy band structures of graphene and N-Ta$_2$O$_5$ layers, and the tendency of charge transfer between layers. The blue dots present for the ionized acceptor centers, while hollow dots stand for holes.

To define the impact of a photodetector on the performance and speed, the rise time has been characterized. Rise time was measured using a low-noise current amplifier (DLPCA-200, FEMTO), and an oscilloscope to monitor the temporal dynamics of the photocurrent under different illumination power. To obtain the ultra-fast response, an acousto-optic modulators (AOM) using a TeO$_2$ crystal produced ultrafast laser pulses from a continuous-wave laser with the rise time of 20 ns. This is the limitation of our transient setup. The photo-

current appears periodically (Fig. 4a, inset) with the pulse duration of 6.3 µs under the 940 nm laser illumination, $V_{DS} = 0.5$ V, and $V_{BG} = -7$ V at room temperature. The temporal dynamics of the positive and negative photocurrent displays the same behavior. For the device with an active area of $W \times L = 20 \times 10$ µm^2, the rise time is estimated to be ~125 ns (from 10 to 90% of the peak photocurrent), while the recovery time is 41 µs (from 90 to 10% of the peak photocurrent). The signal in Fig. 4a shows an ultrafast rise time. The increasing of photocurrent with the illumination time can be fitted to an exponential function with two time constants: $I_{ph} = I_0 - I_1 \exp(-t/\tau_1) - I_2 \exp(-t/\tau_2)$, in which τ_1 is ~20 ns, and τ_2 is 325 ns. The short rise time, τ_1, represents a fast transit time of holes to electrodes, whereas the longer time constant, τ_2, corresponds to the hole transfer time from an accepter center to graphene. Similarly, the decreasing of photocurrent with time when the light is turned off can be fitted to an exponential function: $I_{pH} = I_1 \exp(-t/\tau_3) + I_2 \exp(-t/\tau_4)$ with two decay time constants, $\tau_3 = 500$ ns, and $\tau_4 = 45$ µs. The short decay time constant, τ_3, can be attributed to the time for charge carriers transferring back to the N-Ta$_2$O$_5$ layer because it is similar to τ_2. The slowest time τ_4 may represent the lifetime of ionized acceptor centers. Using the e-beam evaporation to make the N-Ta$_2$O$_5$ light-absorbing layer, fast dynamics including the response and the recovery time of the photocurrent have been obtained. These values are orders of magnitude faster than those from previous reports.[7,9–11,14,16] Extra reset gate-voltage pulses may be required for fast switching performance (faster than 45 µs) of these devices. Nevertheless, the speed reported here is more than sufficient for many imaging applications.

The rise time of the devices in the MIR is slower compared with those from the visible to NIR region (Fig. 4b). The rise time at 10.6 µm shows two components. The fast component is faster than 1 ms (limitation of the test system), and the longer component is 300 ms. The photo-responsivity of the devices strongly depends on the concentration of the acceptor centers. In the N-Ta$_2$O$_5$ thin layer, a broad band of defects is created with the maximum absorption at ~0.9 eV above the VB, and a long tail extending to the MIR region (Fig. S5, ESI†). The density of states of defects in the MIR region is lower than that in the NIR region. Thus, the electronic transport turns from a band-like regime at high carrier concentration in the NIR region to a hopping regime at low carrier concentration in the MIR region. As a result, the photo-responsivity at low acceptor density is slower in the MIR region, which is consistent with previous studies.[45,46]

To evaluate the capability of weak light detection of a photodetector, two key metrics including the specific detectivity (D^*) and the noise equivalent power (NEP) have been examined by considering the $1/f$ noise, shot noise, and thermal noise. The power spectral density of $1/f$ noise in the dark of the graphene-Ta$_2$O$_5$ heterostructure structure and graphene only is shown in Fig. 3b. The noise-power spectral density exhibits the $1/f$ behavior. The noise-power spectral density of the graphene-Ta$_2$O$_5$ heterostructure with an Al$_2$O$_3$ layer covered the entire surface is reduced by almost two orders of magnitude when compared to a device with only graphene (Fig. 3b). The improvement of the device is originated from the top Al$_2$O$_3$ layer which protects graphene as well as the N-Ta$_2$O$_5$ absorbing layer from moisture and other contaminations.[47] A similar structure with an encapsulated Al$_2$O$_3$ layer in the literature also presented a significant improvement of the $1/f$ noise.[48] A detail of the calculations for these noises is presented in the ESI.† The frequency-dependence of the noise current for the photodetector at room temperature
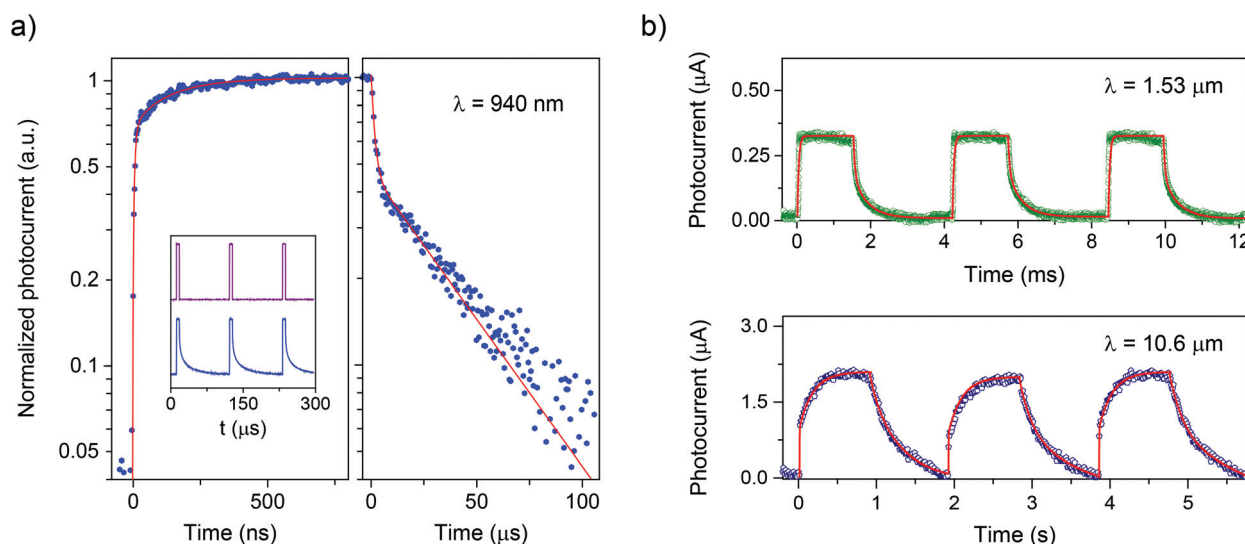
Fig. 4 Photocurrent response of graphene-Ta$_2$O$_5$ photodetector ($W \times L = 20 \times 10$ µm^2) to on/off illumination. (a) The transient photo-response of the device for an illumination at wavelength of 940 nm under $V_{DS} = 0.5$ V and $V_{BG} = -7$ V. The photocurrent response shows fast response and recovery time. The red curves are the best fitting to the data with a bi-exponential function (left panel), and bi-exponential decay function (right panel). (b) The photocurrent response of the device for different illumination at wavelength of 1.53 µm (top panel), and at wavelength of 10.6 µm (bottom panel).
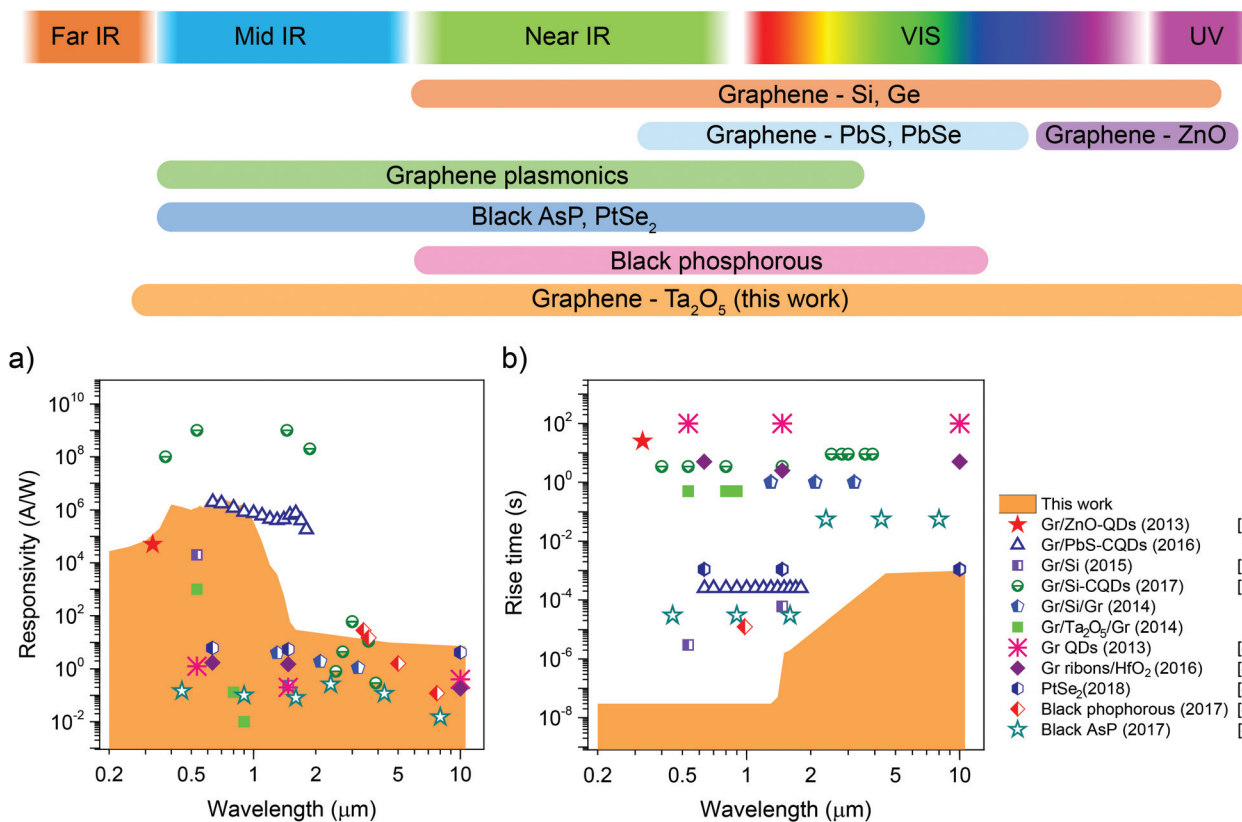
Fig. 5 Comparison photodetectors operated at different wavelengths based on 2D materials including graphene, black AsP, PtSe$_2$, black phosphorous. Comparison the current results with those reported in the literature for the (a) photo-responsivity (b) rise time is provided.

was measured under V_{DS} = 0.5 V and V_{BG} = 7 V at the modulation frequency of 1 Hz. The NEP values $\left(\text{NEP} = \sqrt{S_I(1/f) + S_I(\text{shot}) + S_I(\text{thermal})}/R\right)$ are achieved as low as 7.9×10^{-16} and 2.2×10^{-10} (W Hz$^{-1/2}$) in the UV-to-NIR region and the MIR region, respectively (Fig. 3c, inset). This yields specific detectivity values, $D^* = \sqrt{S}/\text{NEP}$, ($S$ is the area of the detector) in the order of 2.2×10^{12} and 0.8×10^7 (Jones) for the UV-to-NIR and MIR regions, respectively (Fig. 3c, inset). The small values of NEP, or large values of D^* indicate that graphene-Ta$_2$O$_5$ heterostructure photodetectors can be well used for weak light detection from deep-UV to MIR region.

Photo-responsivity and rise time for photodetectors based on 2D materials including graphene, graphene quantum dots,[49] graphene nanoribbons,[50] PtSe$_2$,[51] black phosphorous,[52] black arsenic phosphorus[46] are shown in Fig. 5. It is clear that the photo-responsivity of the graphene-Ta$_2$O$_5$ heterostructure is similar to the graphene-CQD photodetectors, but the rise time is orders of magnitude faster than other photodetectors based on 2D-materials.

Experimental section

Photodetector fabrication

The graphene-Ta$_2$O$_5$ heterostructure photodetectors were fabricated on a p-doped Si wafer (1–10 Ω cm). The surface of the Si

wafer was covered by a 300 nm silicon dioxide and patterned with alignment marks. A metal back-gate directly contacting to the Si substrate was designed using photolithography, then a HF buffer etching solution was used to remove the SiO$_2$ area. Metal films of 10 nm Cr and 100 nm Au were deposited using e-beam evaporation. Metal source and drain contacts (Cr/Au with 10/100 nm thickness) for transport measurements were deposited directly onto the wafer by photolithography to form a field effect transistor.[23–25]

The chemical vapor deposition (CVD) monolayer graphene film on a copper foil from Graphenea Inc. was transferred onto the Si/SiO$_2$ substrate.[3] The CVD graphene on the Cu foil was spin-coated by poly-(methyl-methacrylate) (PMMA), then the Cu foil was removed by using 0.3 M ammonium persulfate solution for 2 hours. Graphene with the PMMA film was rinsed with high purity deionized water and transferred onto the Si/SiO$_2$ wafer with metal contacts. The samples were stored in vacuum for 12 hours to ensure good adhesion. The sample was baked at 120 °C for 15 minutes, then the PMMA was cleaned with acetone for 1 hour. Photolithography and oxygen plasma etching were employed to fabricate graphene patterns between metal contacts. This process eliminates photoresist residue that cannot be removed completely during the lift-off steps. Next, a 10 nm N-Ta$_2$O$_5$ layer was deposited on the top of the CVD graphene by e-beam thermal evaporation with a rate of 0.1 Å per second. The device was covered with a 30 nm

Al_2O_3 film using the atomic layer deposition method at 300 °C. The $N-Ta_2O_5$ and Al_2O_3 layers cover the entire surface, and photolithography was used to redefine source, drain, and back-gate contacts. These layers were then removed by SF_6 plasma dry-etching.

A schematic diagram of the graphene-Ta_2O_5 heterostructure photodetector is shown in Fig. 1a. The length, L, and width, W, of the active area have been varied. AFM and SEM images of our graphene-Ta_2O_5 heterostructure are shown in Fig. S1 and S3.†

Photodetector characterization

The electrical and optical characteristics were examined by two Keithley 2400 source-meter units. The first unit, a Keithley 2400, is used to control the back-gate voltage, V_{BG}. The second unit, a Keithley 2450, is used to set a constant voltage between drain and source, V_{DS}, and to measure the drain current, I_{DS}. The electrical signal also is analyzed by a lock-in amplifier (SR830). Several light sources have been employed in the experiments. In the UV-to-NIR region, laser diodes operating at 532 and 940 nm, a UV-VIS-NIR broadband light source with a wavelength range from 190 nm to 2.6 μm (Edmund, deuterium/tungsten lamp, #87-300), and a fiber laser lasing at 1.53 μm have been used. A set of Edmunds bandpass filters with a narrow bandwidth is employed to select desired wavelengths from 200 nm to 1600 nm. For MIR experiments, a CO_2 laser operating at 10.6 μm and a quantum cascade laser lasing at 4.55 μm are used.

To obtain a low and precise power of the light sources on devices, a beam expander and a number of optical elements have been used (Fig. S7†). The beam expander increases the diameter of a collimated beam. A diaphragm with a 5 mm diameter is used to form uniformly the intensity distribution of the light source. The uniform intensity distribution has been verified using a photodetector with a 10 μm pinhole entrance on a two dimensional stage. A half-wave plate and a polarizing beam-splitter are used to control the power of laser beams. To control the power of incoherent light sources, a number of neutral density filters have been employed. The light sources cover the entire graphene FET photodetector. By knowing the active size as well as photon flux, the power of the light incident upon the graphene-Ta_2O_5 heterostructure photodetectors can be estimated. We have checked polarization properties of the photodetectors by rotating the device. No polarization effect has been observed in the photodetectors. In addition to these experiments, the low-frequency noise spectra were acquired by a single-channel 100 kHz FFT spectrum analyzer (SR770).

Conclusions

In summary, we have fabricated and demonstrated graphene-Ta_2O_5 heterostructure photodetectors with improved photo-responsivity and ultrafast response speed. The structure extends the photo-detection of graphene hybrid phototransis-tors from the UV-visible region into the MIR region. The current work has established the development of high-performance optoelectronic devices based on two-dimensional heterostructure, demonstrating for the first time the added value provided by merging of these two important materials – graphene for optoelectronic and Ta_2O_5 for microelectronics, photonics and solar energy applications.

Conflicts of interest

There are no conflicts to declare.

Acknowledgements

Notes and references

1 F. H. L. Koppens, T. Mueller, P. Avouris, A. C. Ferrari, M. S. Vitiello and M. Polini, *Nat. Nanotechnol.*, 2014, **9**, 780–793.

2 F. Wang, Y. B. Zhang, C. S. Tian, C. Girit, A. Zettl, M. Crommie and Y. R. Shen, *Science*, 2008, **320**, 206–209.

3 K. S. Novoselov, D. Jiang, F. Schedin, T. J. Booth, V. V. Khotkevich, S. V. Morozov and A. K. Geim, *Proc. Natl. Acad. Sci. U. S. A.*, 2005, **102**, 10451–10453.

4 A. Urich, K. Unterrainer and T. Mueller, *Nano Lett.*, 2011, **11**, 2804–2808.

5 J. Park, Y. H. Ahn and C. Ruiz-Vargas, *Nano Lett.*, 2009, **9**, 1742–1746.

6 I. Nikitskiy, S. Goossens, D. Kufer, T. Lasanta, G. Navickaite, F. H. L. Koppens and G. Konstantatos, *Nat. Commun.*, 2016, **7**, 11954.

7 C. H. Liu, Y. C. Chang, T. B. Norris and Z. H. Zhong, *Nat. Nanotechnol.*, 2014, **9**, 273–278.

8 C. R. Kagan, E. Lifshitz, E. H. Sargent and D. V. Talapin, *Science*, 2016, **353**, aac5523.

9 G. Konstantatos, M. Badioli, L. Gaudreau, J. Osmond, M. Bernechea, F. P. G. de Arquer, F. Gatti and F. H. L. Koppens, *Nat. Nanotechnol.*, 2012, **7**, 363–368.

10 Z. H. Sun, Z. K. Liu, J. H. Li, G. A. Tai, S. P. Lau and F. Yan, *Adv. Mater.*, 2012, **24**, 5878–5883.

11 Z. Y. Ni, L. L. Ma, S. C. Du, Y. Xu, M. Yuan, H. H. Fang, Z. Wang, M. S. Xu, D. S. Li, J. Y. Yang, W. D. Hu, X. D. Pi and D. R. Yang, *ACS Nano*, 2017, **11**, 9854–9862.

12 C. R. Dean, A. F. Young, I. Meric, C. Lee, L. Wang, S. Sorgenfrei, K. Watanabe, T. Taniguchi, P. Kim, K. L. Shepard and J. Hone, *Nat. Nanotechnol.*, 2010, **5**, 722–726.

13 X. C. Yu, Y. Y. Li, X. N. Hu, D. L. Zhangg, Y. Tao, Z. X. Liu, Y. M. He, M. A. Haque, Z. Liu, T. Wu and Q. J. Wang, *Nat. Commun.*, 2018, **9**, 4299.

14 W. H. Guo, S. G. Xu, Z. F. Wu, N. Wang, M. M. T. Loy and S. W. Du, *Small*, 2013, **9**, 3031–3036.

15 Z. F. Chen, Z. Z. Cheng, J. Q. Wang, X. Wan, C. Shu, H. K. Tsang, H. P. Ho and J. B. Xu, *Adv. Opt. Mater.*, 2015, **3**, 1207–1214.

16 S. Y. Chen, Y. Y. Lu, F. Y. Shih, P. H. Ho, Y. F. Chen, C. W. Chen, Y. T. Chen and W. H. Wang, *Carbon*, 2013, **63**, 23–29.

17 R. Marschall and L. Z. Wang, *Catal. Today*, 2014, **225**, 111–135.

18 V. A. Gritsenko, T. V. Perevalov, V. A. Voronkovskii, A. A. Gismatulin, V. N. Kruchinin, V. S. Aliev, V. A. Pustovarov, I. P. Prosvirin and Y. Roizin, *ACS Appl. Mater. Interfaces*, 2018, **10**, 3769–3775.

19 T. K. Gu, T. Tada and S. Watanabe, *ACS Nano*, 2010, **4**, 6477–6482.

20 Y. Freeman, *Tantalum and Niobium-Based Capacitors: Science, Technology, and Applications*, Springer, 1st edn, 2018.

21 N. Alimardani, S. King, B. L. French, C. Tan, B. P. Lampert and J. F. Conley, *J. Appl. Phys.*, 2014, **116**, 024508.

22 H. Kozawaguchi, B. Tsujiyama and K. Murase, *Jpn. J. Appl. Phys.*, 1982, **21**, 1028–1031.

23 Y. Wang, V. X. Ho, Z. N. Henschel, M. P. Cooney and N. Q. Vinh, *ACS Appl. Nano Mater.*, 2021, **4**, 3647–3653.

24 Y. Wang, V. X. Ho, Z. N. Henschel, P. Pradhan, L. Howe, M. P. Cooney and N. Q. Vinh, *Proc. SPIE*, 2020, **11503**, 1150306.

25 V. X. Ho, Y. Wang, M. P. Cooney and N. Q. Vinh, *Proc. SPIE*, 2018, **10729**, 1072907.

26 M. C. Lemme, F. H. L. Koppens, A. L. Falk, M. S. Rudner, H. Park, L. S. Levitov and C. M. Marcus, *Nano Lett.*, 2011, **11**, 4134–4137.

27 E. C. Peters, E. J. H. Lee, M. Burghard and K. Kern, *Appl. Phys. Lett.*, 2010, **97**, 193102.

28 J. Bullock, M. Amani, J. Cho, Y. Z. Chen, G. H. Ahn, V. Adinolfi, V. R. Shrestha, Y. Gao, K. B. Crozier, Y. L. Chueh and A. Javey, *Nat. Photonics*, 2018, **12**, 601–607.

29 H. Shin, S. Y. Park, S. T. Bae, S. Lee, K. S. Hong and H. S. Jung, *J. Appl. Phys.*, 2008, **104**, 116108.

30 T. Murase, H. Irie and K. Hashimoto, *J. Phys. Chem. B*, 2004, **108**, 15803–15807.

31 R. Ullah, H. Q. Sun, H. M. Ang, M. O. Tade and S. B. Wang, *Ind. Eng. Chem. Res.*, 2013, **52**, 3320–3328.

32 T. Morikawa, S. Saeki, T. Suzuki, T. Kajino and T. Motohiro, *Appl. Phys. Lett.*, 2010, **96**, 142111.

33 W. J. Chun, A. Ishikawa, H. Fujisawa, T. Takata, J. N. Kondo, M. Hara, M. Kawai, Y. Matsumoto and K. Domen, *J. Phys. Chem. B*, 2003, **107**, 1798–1803.

34 K. Yamanaka, S. Sato, M. Iwaki, T. Kajino and T. Morikawa, *J. Phys. Chem. C*, 2011, **115**, 18348–18353.

35 R. J. Bondi, B. P. Fox and M. J. Marinella, *J. Appl. Phys.*, 2017, **121**, 214102.

36 N. Sedghi, H. Li, I. F. Brunell, K. Dawson, R. J. Potter, Y. Guo, J. T. Gibbon, V. R. Dhanak, W. D. Zhang, J. F. Zhang, J. Robertson, S. Hall and P. R. Chalker, *Appl. Phys. Lett.*, 2017, **110**, 102902.

37 G. Shang, P. W. Peacock and J. Robertson, *Appl. Phys. Lett.*, 2004, **84**, 106–108.

38 R. Asahi, T. Morikawa, T. Ohwaki, K. Aoki and Y. Taga, *Science*, 2001, **293**, 269–271.

39 H. Irie, Y. Watanabe and K. Hashimoto, *J. Phys. Chem. B*, 2003, **107**, 5483–5486.

40 R. Jinnouchi, A. V. Akimov, S. Shirai, R. Asahi and O. V. Prezhdo, *J. Phys. Chem. C*, 2015, **119**, 26925–26936.

41 S. Kim, J. Nah, I. Jo, D. Shahrjerdi, L. Colombo, Z. Yao, E. Tutuc and S. K. Banerjee, *Appl. Phys. Lett.*, 2009, **94**, 062107.

42 D. L. Shao, J. Gao, P. Chow, H. T. Sun, G. Q. Xin, P. Sharma, J. Lian, N. A. Koratkar and S. Sawyer, *Nano Lett.*, 2015, **15**, 3787–3792.

43 J. J. Liu, Y. L. Yin, L. H. Yu, Y. C. Shi, D. Liang and D. X. Dai, *Sci. Rep.*, 2017, **7**, 40904.

44 Q. K. Yu, L. A. Jauregui, W. Wu, R. Colby, J. F. Tian, Z. H. Su, H. L. Cao, Z. H. Liu, D. Pandey, D. G. Wei, T. F. Chung, P. Peng, N. P. Guisinger, E. A. Stach, J. M. Bao, S. S. Pei and Y. P. Chen, *Nat. Mater.*, 2011, **10**, 443–449.

45 Q. S. Guo, A. Pospischil, M. Bhuiyan, H. Jiang, H. Tian, D. Farmer, B. C. Deng, C. Li, S. J. Han, H. Wang, Q. F. Xia, T. P. Ma, T. Mueller and F. N. Xia, *Nano Lett.*, 2016, **16**, 4648–4655.

46 M. S. Long, A. Y. Gao, P. Wang, H. Xia, C. Ott, C. Pan, Y. J. Fu, E. F. Liu, X. S. Chen, W. Lu, T. Nilges, J. B. Xu, X. M. Wang, W. D. Hu and F. Miao, *Sci. Adv.*, 2017, **3**, e1700589.

47 M. Kayyalha and Y. P. Chen, *Appl. Phys. Lett.*, 2015, **107**, 113101.

48 S. G. Peng, Z. Jin, D. Y. Zhang, J. Y. Shi, D. C. Mao, S. Q. Wang and G. H. Yu, *ACS Appl. Mater. Interfaces*, 2017, **9**, 6661–6665.

49 Y. Z. Zhang, T. Liu, B. Meng, X. H. Li, G. Z. Liang, X. N. Hu and Q. J. Wang, *Nat. Commun.*, 2013, **4**, 1811.

50 X. C. Yu, Z. G. Dong, Y. P. Liu, T. Liu, J. Tao, Y. Q. Zeng, J. K. W. Yang and Q. J. Wang, *Nanoscale*, 2016, **8**, 327–332.

51 X. C. Yu, P. Yu, D. Wu, B. Singh, Q. S. Zeng, H. Lin, W. Zhou, J. H. Lin, K. Suenaga, Z. Liu and Q. J. Wang, *Nat. Commun.*, 2018, **9**, 1545.

52 M. Amani, E. Regan, J. Bullock, G. H. Ahn and A. Javey, *ACS Nano*, 2017, **11**, 11724–11731.

Electronic Supplementary Information

Graphene-Ta$_2$O$_5$ Heterostructure Enabled High Performance,

Deep-Ultraviolet to Mid-Infrared Photodetection

Vinh X. Ho[1], Yifei Wang[1], Michael P. Cooney[2], and Nguyen Q. Vinh[1]*

[1] Department of Physics and Center for Soft Matter and Biological Physics, Virginia Tech,

Blacksburg, VA 24061, USA

[2] NASA Langley Research Center, Hampton, Virginia 23681, USA

* Corresponding author: vinh@vt.edu; phone: 1-540-231-3158

1. Device fabrication

The chemical vapor deposition (CVD) monolayer graphene on a copper foil from Graphenea Inc. was transferred onto a Si/SiO$_2$ substrate.[1-5] A *p*-doped (1 – 10 Ω.cm) Si wafer under a 300-nm-thick SiO$_2$ layer was used as the back-gate. Metal source and drain contacts (Cr/Au with 10/100-nm thickness) for transport measurements were deposited directly onto the wafer by photolithography to form field effect transistors (FET). The CVD graphene film on top of the wafer was transferred using the poly-(methyl-methacrylate) (PMMA) mediated wet process. The single-layer of graphene was confirmed by the Raman spectroscopy. Using photolithography and oxygen plasma etching processes, graphene films were patterned into different shapes ($W \times L$) on the silicon wafer. L is the gap between drain and contacts (length), and W is the width of the graphene photodetector device (Fig. S1).
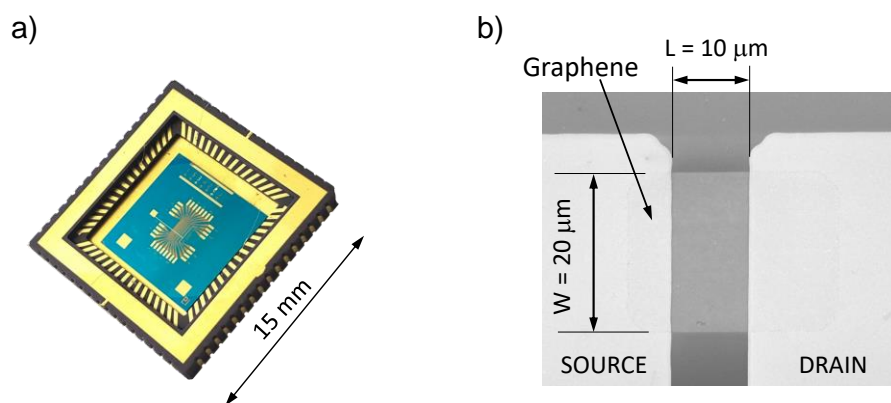

Fig. S1. Images of photodetectors. (a) a picture of photodetector devices including IC package, and (b) a SEM image of an individual photodetector showing the length, L, and the width, W, of the graphene.
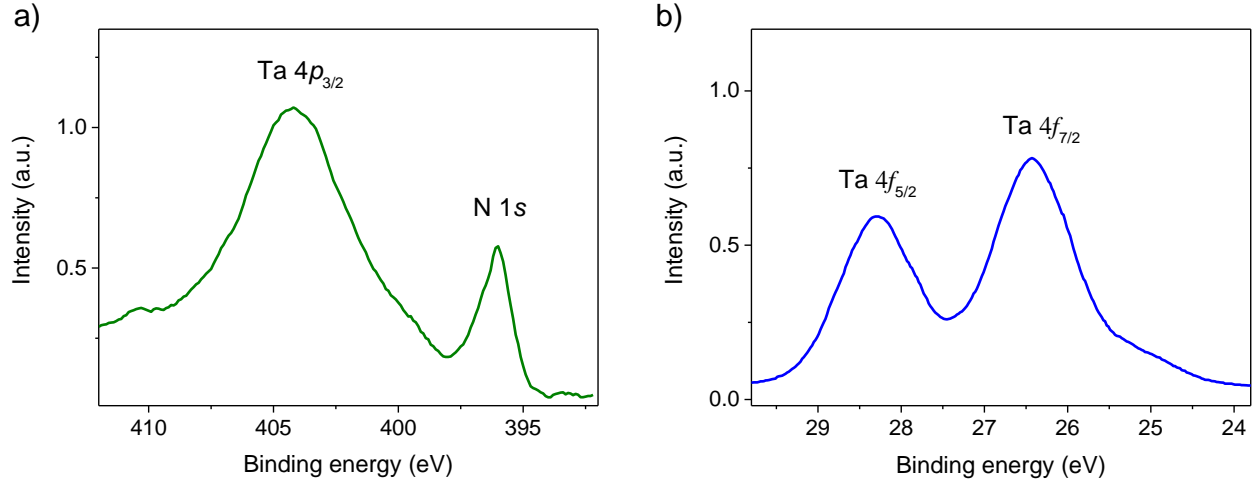
Fig. S2. X-ray photoelectron spectra of N-Ta_2O_5 material (a) Ta $4p_{3/2}$ and N $1s$ peaks, (b) Ta $4f_{5/2}$ and $4f_{7/2}$ peaks.

The orthorhombic-crystalline-structure Ta_2O_5 powder was placed in an alumina crucible and put in the alumina tube furnace. The Ta_2O_5 powder was heated at 750 °C for 2 hours in flowing NH_3 gas at the rate of 100 sccm to obtain the nitrogen-doped tantalum oxide (N-Ta_2O_5) material. The N-Ta_2O_5 was used as a source material to grow the absorber layer on graphene.

The N-Ta_2O_5 material was characterized by X-ray photoelectron spectroscopy (XPS). XPS spectra of the N-Ta_2O_5 material indicate the binding energy of electron for Ta $4p_{3/2}$ and N $1s$ (Fig. S2a). The XPS peaks for N-doped Ta_2O_5 have been reported in the literature.[6, 7] This is the evidence of nitrogen doped Ta_2O_5 at 750 °C. We applied the XPS at the Ta $4f$ shallow core levels in Fig. S2b. There are two Ta $4f_{5/2}$ and $4f_{7/2}$ peaks at 28.3 and 26.4 eV. A tail around 25 eV originates from nitrogen doping to the oxygen vacancy.
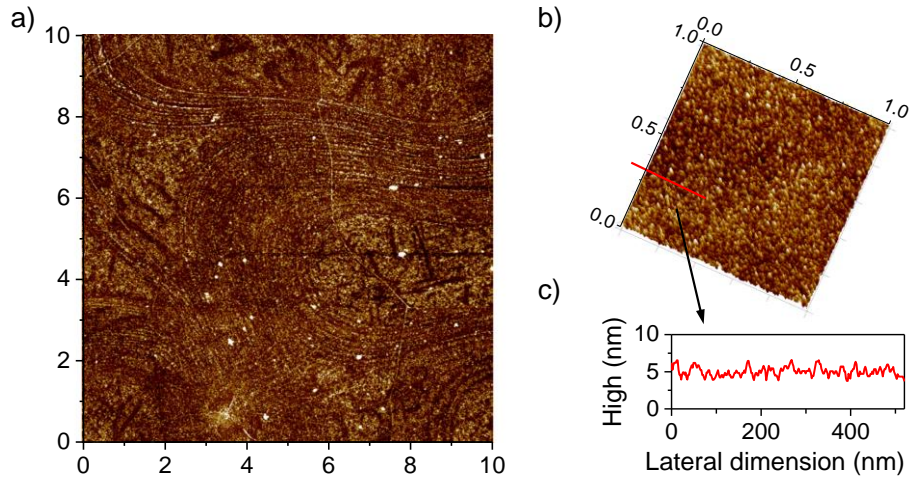
Fig. S3. AFM images of the graphene surface (a), and the N-Ta_2O_5 layer (b) on graphene of photodetector devices.

A 10-nm N-Ta_2O_5 layer was deposited on the CVD graphene by electron-beam thermal evaporation with a slow rate of 0.1 Å/s. This layer acts as a photon absorption material, and contains electron acceptor centers. Then the device was covered with a 30-nm Al_2O_3 dielectric layer using the thermal atomic layer deposition method (ALD) at 250 °C to protect the device from the ambient environment. Figure S1 shows an image of the graphene-Ta_2O_5 photodetector

devices (left) and a scanning electron microscope (SEM) image (right) of an individual photodetector in the main chip.

To verify the quality of the graphene as well as the N-Ta_2O_5 thin film, atomic force microscope (AFM) experiments have been performed. Fig. S3a shows an AFM image of the graphene surface with a size of 10 × 10 μm^2 after the PMMA cleaning process. The graphene surface is homogenous, and there are only a few white dots on the graphene surface in the AFM image. These white dots were originated from PMMA residues, thus almost PMMA residuals were removed in our photodetector devices. An AFM image in Fig. S3b in a short scanning range illustrates the homogeneity of the N-Ta_2O_5 layer with a height of 10 nm.

2. Raman spectrum

To evaluate the quality of graphene after the transferring process, the Raman spectroscopy has been employed. A Raman spectrum (Fig. S4) was obtained by using a WITec UHTS 300 micro-Raman spectrometer equipped with a CCD detector and a 100× objective lens (NA 0.90). The graphene sample was excited by a laser operating at 663.1-nm wavelength. Fig. S4 shows the Raman spectrum of a CVD monolayer graphene on Si/SiO_2. The Raman spectrum shows two main peaks at ~ 1585 cm^{-1} (G line) and ~ 2690 cm^{-1} (2D line). The 2D line is narrow and consists of a single component with a FWHM of 33 cm^{-1}. The intensity ratio of the 2D and G lines, I_{2D}/I_G, is 6.8. The high value confirms a high quality of the graphene layer in the photodetector.[8] The D band around ~ 1350 cm^{-1} (orange box) from graphene defects originating from the graphene transfer process was not observed.[9] These fingerprints provide key evidence of the high-quality of the CVD monolayer graphene, and the efficient transfer process of graphene.
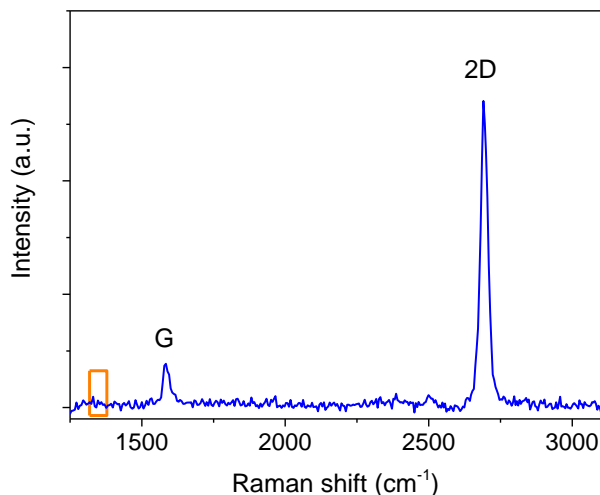

Fig. S4. The Raman spectrum of a CVD monolayer graphene on Si/SiO_2.

3. Absorption measurements

The absorption spectra of the N-Ta_2O_5 material have been recorded from the deep ultraviolet (UV) to mid-infrared (MIR) region (Fig. S5). The Fourier-transform infrared spectroscopy (FTIR) spectrum of the material was recorded on a Nicolet iS50 FTIR spectrometer with a KBr beam splitter (Fig. S5a). The FTIR spectrometer was purged with nitrogen gas for 12 hours to eliminate water vapor and CO_2 before performing absorption measurements. The ultraviolet-visible (UV-VIS) absorption spectra were collected on a Shimadzu UV-3101PC UV-VIS-NIR spectrophotometer. We focus on the optical properties of the N-Ta_2O_5 material using the transmission method. To characterize the optical properties, the material is grown on transmission

substrates. For the visible region, a 100-nm N-Ta$_2$O$_5$ material was grown on an α-sapphire thin wafer. Sapphire material has a large bandgap of 8.8 eV,[10] and a wide optical transmission band from the UV to near-infrared (NIR) region. For the infrared region, the material was grown on a thin silicon wafer. To obtain absorption spectra of the material, their substrates have been used for background signals. The configuration of our absorption experiments has been provided in the insets in Fig. S5. UV-VIS absorption spectra of Ta$_2$O$_5$ and N-Ta$_2$O$_5$ materials have been shown in Fig. S5b. The Tantalum (V) oxide (Ta$_2$O$_5$) with 99.99% was purchased from Sigma Aldrich.
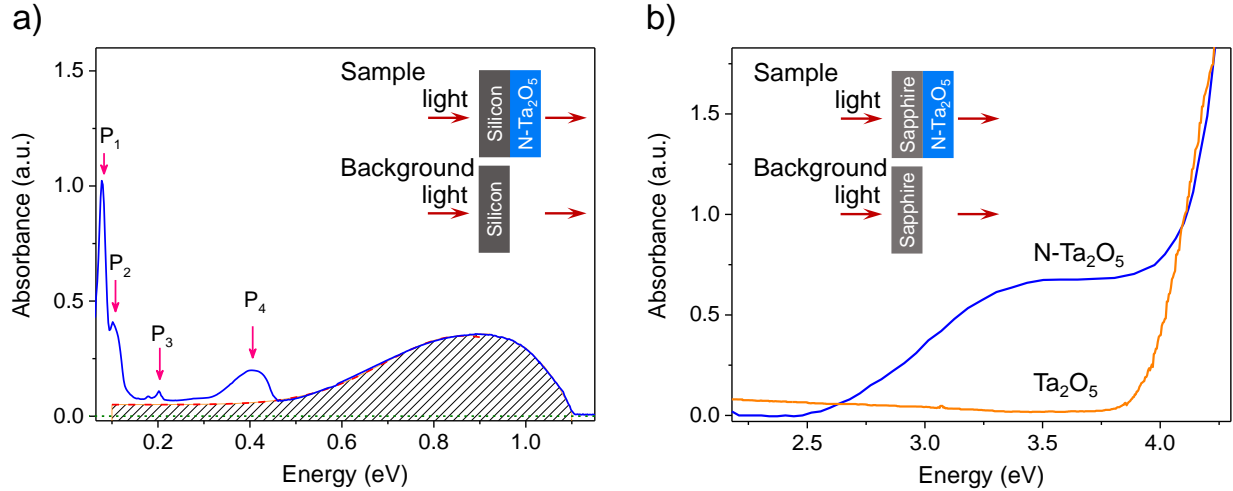
Fig. S5: Absorption spectra of the N-Ta$_2$O$_5$ material used in this work. The absorption spectrometers were purged with nitrogen gas to eliminate the contamination of water vapor and CO$_2$. (a) FTIR spectrum of the N-Ta$_2$O$_5$ material on silicon. The red dash-line curve is a Gaussian fitting curve with the peak position over 0.9 eV for the low energy part. Several peaks (P1 to P4) at the low energy part come from vibrational modes in the material. (b) UV-VIS spectra of Ta$_2$O$_5$ and N-Ta$_2$O$_5$ materials on sapphire.

The absorption spectrum of N-Ta$_2$O$_5$ in the NIR region is shown a shoulder at around 0.9 eV, which comes from acceptor centers, and a long tail extending to the MIR region. The red dash-line curve is a Gaussian fitting curve with the peak position at ~ 0.9 eV. The broad band of defect levels near the valence band of N-Ta$_2$O$_5$ is supported by calculations of the density-functional theory (DFT).[11, 12] The calculation provides the atomic structure and density of states (DOS) of the defect states of nitrogen-doped Ta$_2$O$_5$. This report showed that the substitution of oxygen atoms by nitrogen atoms will remove the oxygen vacancy defect states in the band gap of Ta$_2$O$_5$ and leaving nitrogen defect states near the valence band of Ta$_2$O$_5$. Therefore, the infrared performance of our photodetector originates from the ionization of acceptor centers with their energy above the valance band. Several peaks (P$_1$ to P$_4$) at the low energy part come from vibrational modes in the material, indicating the formation of the Ta$_2$O$_5$ material (they are not electronic transitions). These peaks in the absorption spectrum do not involve to the photocurrent. The absorption bands, P$_1$, at 0.05-0.10 eV (400-800 cm^{-1}) are corresponding to Ta-O-Ta and Ta-O stretching vibrational modes.[13] The peak, P$_2$, at 0.11 eV (~ 890 cm^{-1}) is assigned with the octahedral units and Ta suboxides. The peak, P$_3$, at 0.20 eV (1638 cm^{-1}) comes from the in-plane bending vibrations of the Ta-OH groups.[14] The broad peak, P$_4$, around 0.42 eV (3400 cm^{-1}) corresponds to the stretching frequency of O-H groups.[13, 14] The absorption peaks from the vibrational modes originated from the formation of the N-Ta$_2$O$_5$ material do not involve in the photo-response process and thus, we do not discuss the intensity of these peaks.

The absorption of the N-Ta$_2$O$_5$ material at the MIR region (low energy part) is a combination of the absorption of defects and vibrational modes of the material (Figure S5b). The defects

cooperate with the photo-response process. The vibration modes (P_1, P_2, P_3, P_4) in the absorption spectrum come from of the N-Ta$_2$O$_5$ material. Thus, we need to extract the absorption contribution of the defects. Gaussian function has been used to extract the contribution of the defects in the absorption spectrum. We focused on the MIR region, and this part is not influenced by the absorption of the silicon substrate (E_{gap} = 1.1 eV). The Gaussian fitting curve can extract the low energy part of the absorption peak. In addition to this, the band gap of the N-Ta$_2$O$_5$ material becomes narrower (Figure S5b).

## 4. Electrical and optical measurements

The electrical and optical properties were characterized in a broadband wavelength range at room temperature. A schematics for electrical measurements is shown in Fig. S6 using two Keithley 2400 source-meter units. A source-meter (Keithley 2400) is employed to control the back-gate voltage, V_{BG}. Other source-meter unit (Keithley 2450) is used to set a constant voltage between drain and source, V_{DS}, and to measure the drain current, I_{DS}. To cover a broadband wavelength range from the deep-UV to MIR region, a number of light sources have been used. In the UV-to-NIR region, a UV-VIS broadband light source with a wavelength range from 190 nm to 2.6 μm (Edmund, Deuterium/Tungsten lamp, #87-300), laser diodes operating at 532 and 940 nm, and a fiber laser lasing at 1.53 μm have been employed. For MIR experiments, a quantum cascade laser lasing at 4.55 μm, and a CO$_2$ laser operating at 10.6 μm are used.
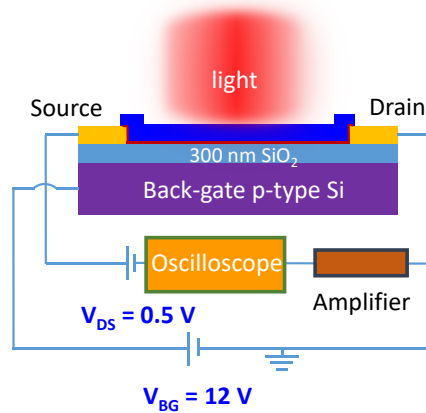
Fig. S6. A Schematic diagram for electrical measurements. A voltage of 0.5 V was applied between drain and source contacts (V_{DS}) using a Keithley 2450 source-meter unit. The back-gate voltage (V_{BG}) was varied from -30 to 30 V with a Keithley 2400 unit. The photocurrent can be collected with a lock-in amplifier, an oscilloscope, or the source-meter unit (Keithley 2450).

To obtain a low and precise power of the light sources on devices, a beam expander has been used. A set of two lenses with f_1 = 25 mm and f_2 = 500 mm (Fig. S7) increases the diameter of a collimated beam. A diaphragm with a 5-mm diameter is used to form the light source with a uniform intensity distribution. A relatively large size of the beam former ensures that we can obtain a correct value of the total power of the beam, and the beam does not contain a significant amount of diffracted light. To verify the uniform intensity distribution, a photodetector with a 10-μm pinhole entrance on a two dimensional stage was used to measure the beam profile. The photon flux of the light sources is measured precisely at the position of our devices with a black anodized aluminum pinhole (1 mm in diameter). A half-wave plate and a polarizing beam-splitter are used to control the power of laser beams. To control the power of incoherent light sources, several sets of Thorlabs neutral density filters have been employed. The light sources cover the entire

graphene FET photodetector. The system allows us to estimate precisely low power of a collimated beam on the graphene-Ta_2O_5 heterostructure photodetectors.[15]
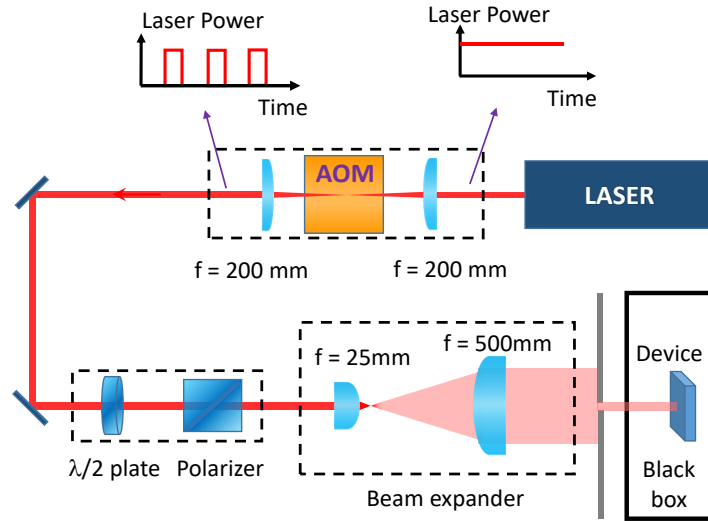
Fig. S7. Optical setup for ultra-fast photo-response measurements. The system consists of an Acousto-optic modulator (AOM), a half-wave plate, a polarizer beam splitter, and lenses. Sample is put in a black box to prevent random light from ambient.

5. Carrier mobility in graphene
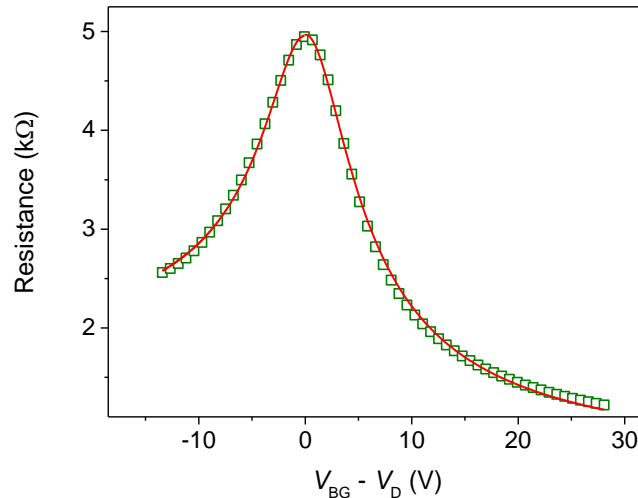
Fig. S8. Resistance – voltage transfer characteristics of a graphene device with N-Ta_2O_5 film (L = 30 μm, W = 30 μm) at room temperature under V_{DS} = 0.1 V.

We determine the mobility, μ, of carriers in graphene from the transfer characteristic curve. The contact resistance, R_c, on a level with the graphene channel resistance, R_{ch}, is estimated from the total device resistance, $R = V_{DS}/I_D$. The mobility of carriers in the graphene device can be extracted by fitting the resistance – voltage (R-V) characteristic curve (Figure 1) in the following form.[16-18]

$$R = 2R_c + R_{ch} = 2R_c + \frac{L}{Wq\mu}\frac{1}{\sqrt{n_0{}^2 + n_g{}^2}} \,, \tag{S1}$$

where $L = 30$ μm and $W = 30$ μm are the length and width of the graphene channel, respectively, q is the charge of electron, n_0 is the carrier density resulting from charged impurities at the interface between graphene and the SiO$_2$ dielectric material, $n_g = \frac{C_G}{q}(V_{BG} - V_D)$ is the density of charged carriers generated by a voltage on the back-gate away from the charge neutrality point voltage, V_D, (the Dirac point), $C_G = \frac{\varepsilon\varepsilon_0}{d}$ is the gate capacitance per unit area with d being the thickness of the SiO$_2$ dielectric material, ε_0 is the vacuum permittivity, and $\varepsilon \sim 3.9$ is the dielectric constant of SiO$_2$.[19] The capacitance of the 300-nm SiO$_2$ dielectric layer is ~11.5 nF/cm^2. The red curve in Fig. S8 presents the best fit to the R-V characteristic data using Eq. S1. We obtain the carrier mobility in graphene of ~4890 cm^2/(V·s).

6. Dependence of responsivity on the back-gate voltage

The photo-responsivity of the graphene-Ta$_2$O$_5$ heterostructure photodetector can be estimated from the photocurrent and the illumination power. The illumination power was measured with a power meter, and the photocurrent was collected with a lock-in amplifier, an oscilloscope, or the source-meter unit (Keithley 2450). Fig. S9 shows the photo-responsivity of the graphene-Ta$_2$O$_5$ heterostructure photodetector ($W \times L = 30 \times 30$ μm^2) as a function of the back-gate voltage, V_{BG}, under 940-nm excitation and $V_{DS} = 0.5$ V using a lock-in amplifier. Signals collected from source-meter setup and lock-in amplifer are similar. The lock-in setup helps us to have faster measurements.
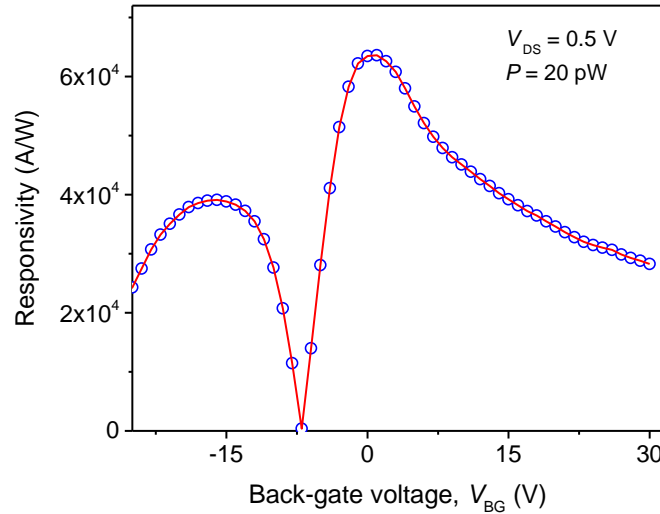

Fig. S9. The photo-responsivity measured with a lock-in system (SR830, Stanford Research) of the graphene-Ta$_2$O$_5$ heterostructure photodetector ($W \times L = 30 \times 30$ μm^2) as a function of the back-gate voltage under 940-nm excitation and $V_{DS} = 0.5$ V.

7. Photocurrent for graphene – Ta$_2$O$_5$ devices with different graphene sheet dimensions

The photocurrent of graphene-Ta$_2$O$_5$ devices strongly depends on geometrical parameters such as the length, L, and width, W, of the active area. We present the photocurrent as a function of back-gate voltage, V_{BG}, and the illumination power, P. Fig. S10 shows photocurrent functions for (a) $W \times L = 10 \times 20$ μm^2; (b) $W \times L = 20 \times 40$ μm^2; (c) $W \times L = 50 \times 100$ μm^2; (d) $W \times L = 100 \times 200$ μm^2; and (e) $W \times L = 200 \times 400$ μm^2. Fig. S11 provides photocurrent functions for (a) $W \times L = 10 \times 10$ μm^2; (b) $W \times L = 10 \times 30$ μm^2; (c) $W \times L = 10 \times 40$ μm^2.
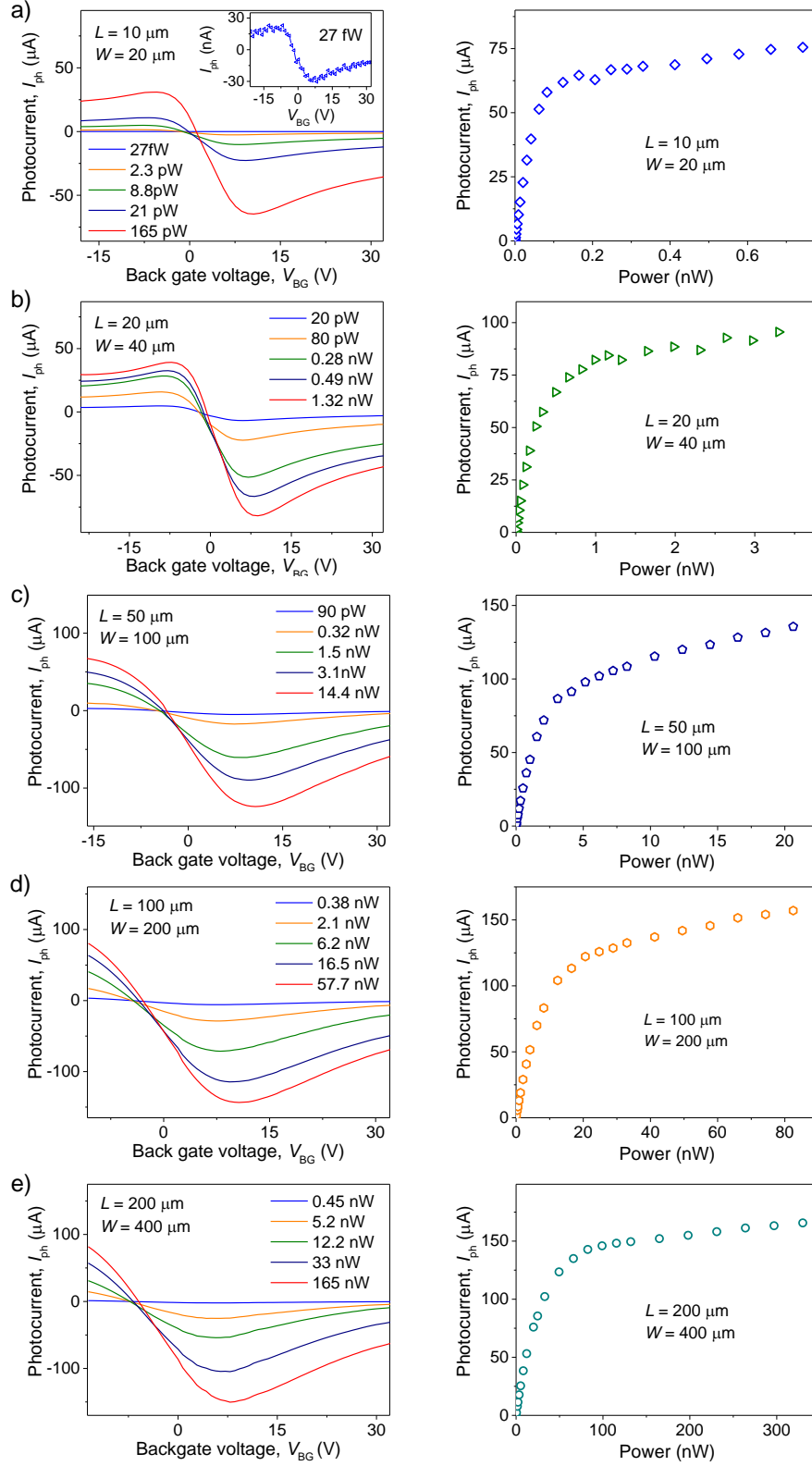
Fig. S10. Photocurrent curves under different illumination powers as a function of back-gate voltage (left), and as a function of illumination power (right) with $V_{BG} \sim 7$ V for (a) $W \times L = 10 \times 20$ μm^2; (b) $W \times L = 20 \times 40$ μm^2; (c) $W \times L = 50 \times 100$ μm^2; (d) $W \times L = 100 \times 200$ μm^2; and (e) $W \times L = 200 \times 400$ μm^2 under 940-nm excitation and $V_{DS} = 0.5$ V.
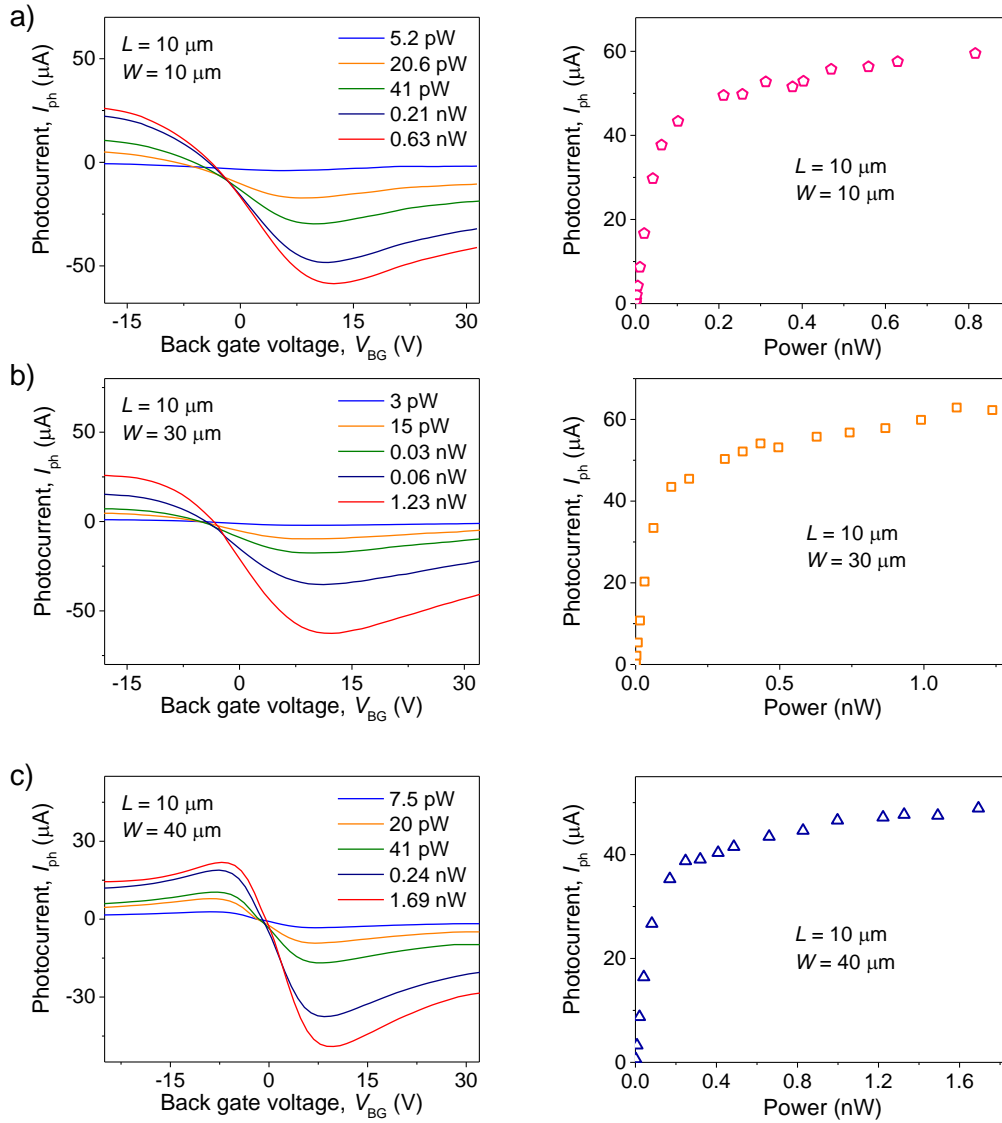
Fig. S11. Photocurrent curves under different illumination powers as a function of back-gate voltage (left), and as a function of illumination power (right) with $V_{BG} \sim 7$ V for (a) $W \times L = 10 \times 10$ μm^2; (b) $W \times L = 10 \times 30$ μm^2; and (c) $W \times L = 10 \times 40$ μm^2 under 940-nm excitation and $V_{DS} = 0.5$ V.

8. Power dependence measurements

The photocurrent, I_{ph}, as a function of illumination power with different illumination wavelengths from the deep-UV to MIR region is shown in Fig. S12.
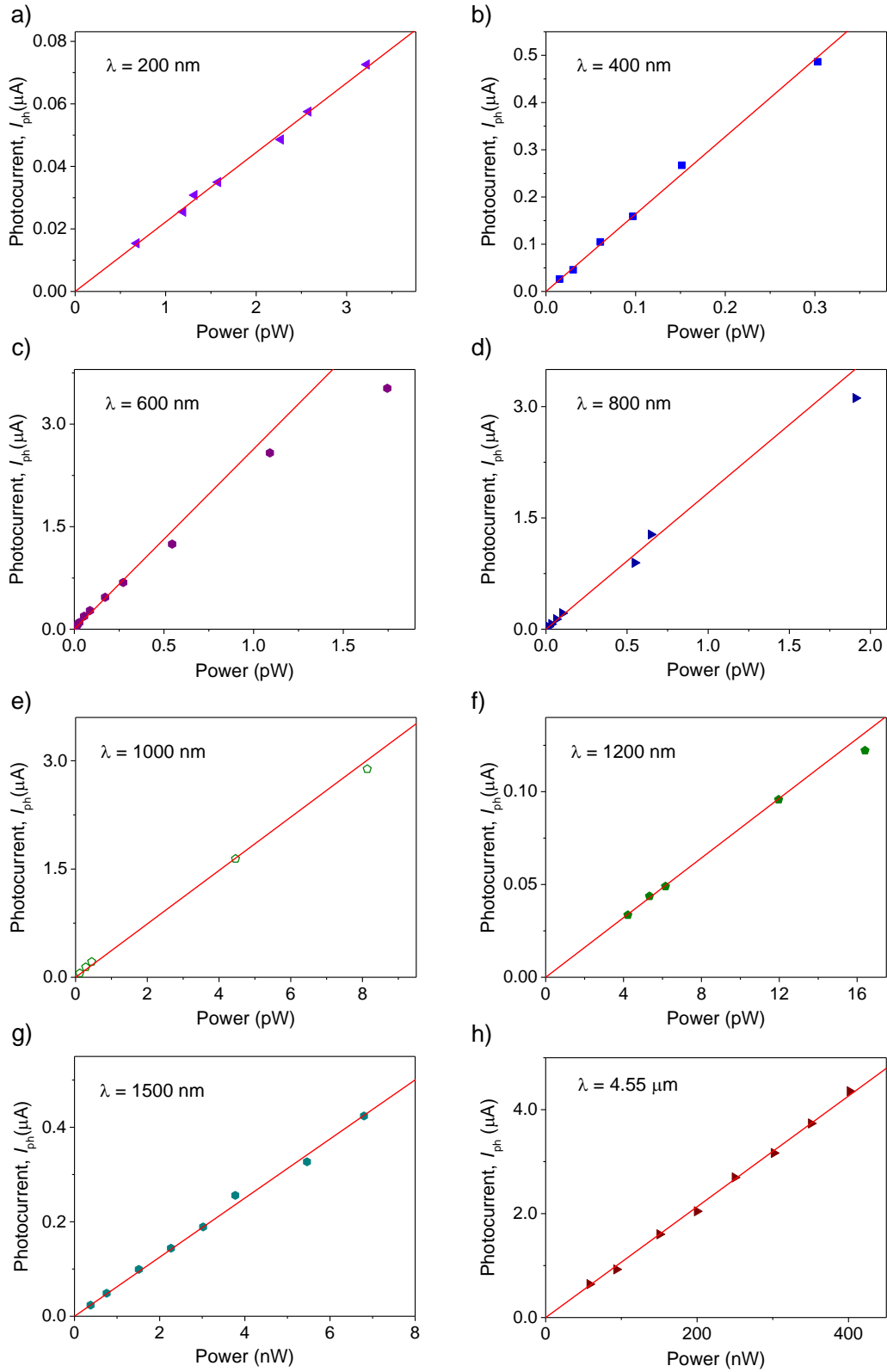
Fig. S12. Photocurrent as a function of illumination power for several light sources with different wavelengths.

9. Noise characterization

For practical applications, the noise-equivalent-power (NEP) as well as the specific detectivity (D^*) are important parameters of a photodetector, which are expressed as

$$D^* = \frac{\sqrt{S \times \Delta f}}{\text{NEP}} \ , \tag{S2}$$

where Δf is the bandwidth in hertz, and S is the area of the device in cm^2. The NEP can be evaluated by considering the power spectral density of $1/f$ noise, shot noise, and thermal noise of graphene-Ta$_2$O$_5$ photodetectors.

a)

b)
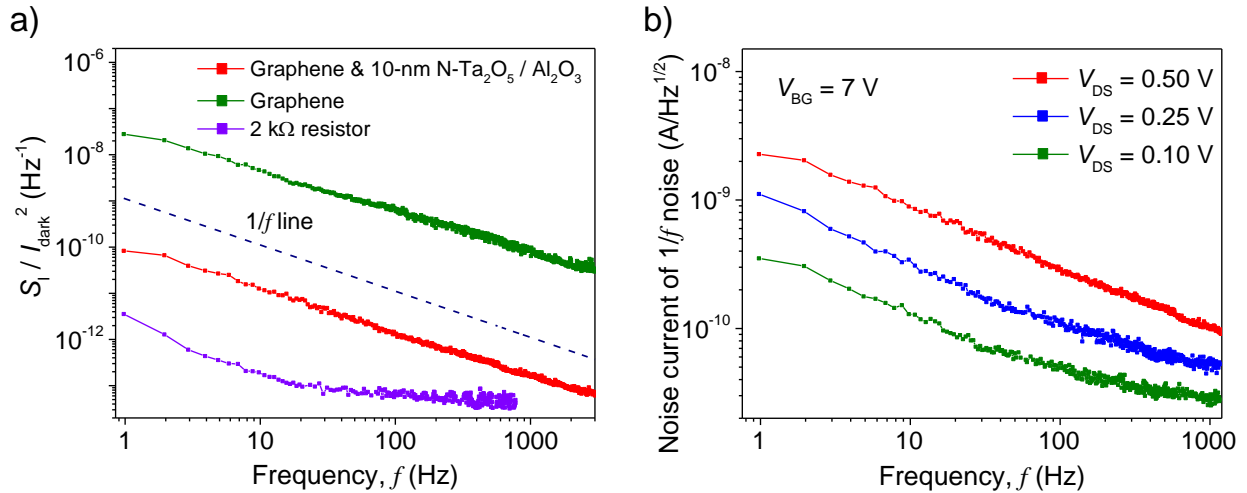
Fig. S13. (a) Normalized noise-power spectral density ($S_\text{I}/I_\text{dark}^2$) of our FET devices with graphene (green curve); the graphene-Ta$_2$O$_5$ photodetector ($W \times L = 20 \times 10$ μm^2) with an encapsulated ALD Al$_2$O$_3$ layer (red curve) at $V_\text{DS} = 0.5$ V and $V_\text{BG} = 7$ V at a modulation frequency of 1 Hz. Background noise of our system was characterized with a 2 kΩ resistor (purple). A guide to the eye of the $1/f$ behavior is shown (dash line with a slope = -1 in the log-log plot). (b) The noise current of $1/f$ noise for the graphene-Ta$_2$O$_5$ photodetector with different drain-source voltages, V_DS.

The noise-power spectral density is characterized using a single-channel 100 kHz FFT spectrum analyzer (SR770) for the graphene-Ta$_2$O$_5$ photodetector with $W \times L = 20 \times 10$ μm^2. The noise-power spectral density was acquired by a current preamplifier with a sampling rate of 1 Hz at $V_\text{DS} = 0.5$ V and $V_\text{BG} = 7$ V. To evaluate the noise-power spectral density, the power spectral density (S_I) of $1/f$ noise (or the Flicker noise) in the dark can be expressed in term of the normalized noise-power spectral density ($S_\text{I}/I_\text{dark}^2$):[20]

$$S_\text{I}(1/f) = \frac{A I_\text{dark}^2}{f^\beta} \ , \tag{S3}$$

where A is the noise amplitude (dimensional less), and β is close to 1. The normalized noise-power spectral density is plotted in Fig. S13a. The spectra are dominated by $1/f$ noise up to 1 kHz. The normalized noise-power spectral density for a graphene field effect transistor device without the N-Ta$_2$O$_5$ layer resembles closely with previous measurements for single-layer graphene devices.[20] Our graphene-Ta$_2$O$_5$ photodetectors encapsulated with an ALD Al$_2$O$_3$ layer reduce noise by two orders of magnitude. Background noise of our system was characterized

with a 2 kΩ resistor. A similar structure with an encapsulated Al_2O_3 layer shows significantly improvement of the $1/f$ noise.[21] The noise current of $1/f$ noise, $\sigma(1/f) = \sqrt{S_I(1/f)}$ depends on the bias between drain and source, V_{DS}. Fig. S13b shows the noise current of $1/f$ noise of the graphene-Ta_2O_5 device for three values of V_{DS}. Thus, we have estimated the NEP value from the power spectral density of $1/f$ noise is ~ 2.9 nA/$\sqrt{Hz}$ under V_{DS} = 0.5 V and V_{BG} = 7 V, at a modulation frequency of 1 Hz.
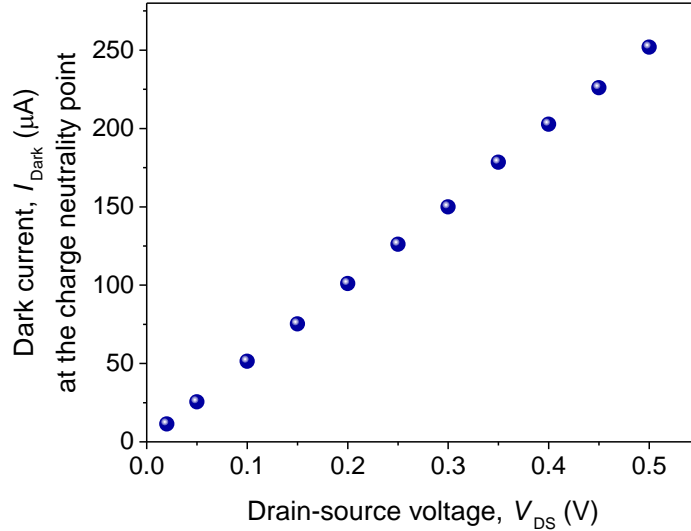
Fig. S14. Dark current at the charge neutrality point as a function of back-gate voltage.
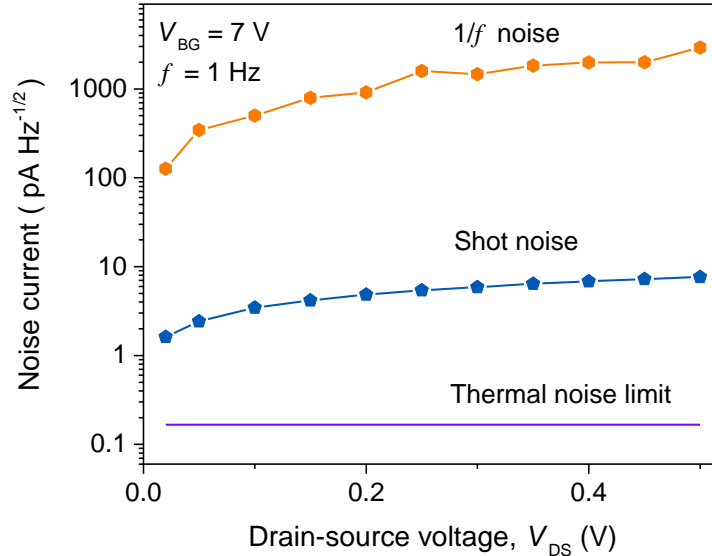
Fig. S15. Noise current of $1/f$ noise, shot noise, and thermal noise of the graphene-Ta_2O_5 photodetector ($W \times L = 20 \times 10$ μm^2) as a function of drain-source voltage, V_{DS}.

12

The shot noise is estimated from the spectral density of shot noise given by:

$$\sigma_I(\text{shot}) = \sqrt{S_I(\text{shot})} = \sqrt{2qI_{\text{dark}}} \,, \tag{S4}$$

where q is the elemental charge, and I_{dark} is the dark current of the device. Fig. S14 shows the dark current, I_{dark}, at the charge neutrality point as a function of back-gate voltage. The calculated spectral density of shot noise is ~ 7.64 (pA/$\sqrt{\text{Hz}}$).

The thermal noise is calculated from the spectral density of thermal noise by using Nyquist's equation:

$$\sigma_I(\text{thermal}) = \sqrt{S_I(\text{thermal})} = \sqrt{4k_B T/R} \,, \tag{S5}$$

where k_B is the Boltzmann's constant, T is the temperature, and R is the differential resistance of the device in the dark. The thermal noise at room temperature is estimated ~ 0.17 (pA/$\sqrt{\text{Hz}}$). The noise current of $1/f$ noise, shot noise, and thermal noise of the graphene-Ta_2O_5 photodetector as a function of drain-source voltage have been presented in Fig. S15.

References

1. K. S. Novoselov, D. Jiang, F. Schedin, T. J. Booth, V. V. Khotkevich, S. V. Morozov and A. K. Geim, *Proc. Natl. Acad. Sci. U. S. A.*, 2005, **102**, 10451-10453.
2. Y. Wang, V. X. Ho, Z. N. Henschel, M. P. Cooney and N. Q. Vinh, *ACS Appl. Nano Mater.*, 2021, **4**, 3647-3653.
3. Y. Wang, V. X. Ho, Z. N. Henschel, P. Pradhan, L. Howe, M. P. Cooney and N. Q. Vinh, *Proc. SPIE*, 2020, **11503**, 1150306.
4. Y. Wang, V. X. Ho, P. Pradhan, M. P. Cooney and N. Q. Vinh, *Proc. SPIE*, 2019, **11088**, 1108809.
5. V. X. Ho, Y. Wang, M. P. Cooney and N. Q. Vinh, *Proc. SPIE*, 2018, **10729**, 1072907.
6. T. Morikawa, S. Saeki, T. Suzuki, T. Kajino and T. Motohiro, *Appl. Phys. Lett.*, 2010, **96**, 142111.
7. T. Murase, H. Irie and K. Hashimoto, *J. Phys. Chem. B*, 2004, **108**, 15803-15807.
8. L. M. Malard, M. A. Pimenta, G. Dresselhaus and M. S. Dresselhaus, *Phys. Rep.*, 2009, **473**, 51-87.
9. M. Her, R. Beams and L. Novotny, *Phys. Lett. A*, 2013, **377**, 1455-1458.
10. R. H. French, *J. Am. Ceram. Soc.*, 1990, **73**, 477-489.
11. N. Sedghi, H. Li, I. F. Brunell, K. Dawson, R. J. Potter, Y. Guo, J. T. Gibbon, V. R. Dhanak, W. D. Zhang, J. F. Zhang, J. Robertson, S. Hall and P. R. Chalker, *Appl. Phys. Lett.*, 2017, **110**, 102902.
12. R. Jinnouchi, A. V. Akimov, S. Shirai, R. Asahi and O. V. Prezhdo, *J. Phys. Chem. C*, 2015, **119**, 26925-26936.
13. J. Y. Zhang, B. Lim and I. W. Boyd, *Thin Solid Films*, 1998, **336**, 340-343.
14. K. Chennakesavulu and G. R. Reddy, *RSC Adv.*, 2015, **5**, 56391-56400.
15. J. R. Mahan, N. Q. Vinh, V. X. Ho and N. B. Munir, *Appl. Opt.*, 2018, **57**, D56-D62.
16. S. Kim, J. Nah, I. Jo, D. Shahrjerdi, L. Colombo, Z. Yao, E. Tutuc and S. K. Banerjee, *Appl. Phys. Lett.*, 2009, **94**, 062107.
17. K. Chen, X. Wan, D. Q. Liu, Z. W. Kang, W. G. Xie, J. Chen, Q. Miao and J. B. Xu, *Nanoscale*, 2013, **5**, 5784-5793.
18. N. Wang, Z. H. Ma, C. Ding, H. Z. Jia, G. R. Sui and X. M. Gao, *Energy Technol.*, 2020, **8**, 1901466.
19. M. Baklanov, M. Green and K. Maex, *Dielectric Films for Advanced Microelectronics*, John Wiley & Sons, Ltd, 2007.
20. M. Kayyalha and Y. P. Chen, *Appl. Phys. Lett.*, 2015, **107**, 113101.
21. S. G. Peng, Z. Jin, D. Y. Zhang, J. Y. Shi, D. C. Mao, S. Q. Wang and G. H. Yu, *ACS Appl. Mater. Interfaces*, 2017, **9**, 6661-6665.